Nucleation and growth of sub-3 nm particles in the polluted urban atmosphere of a megacity in China

Huan Yu[1,2,*], Luyu Zhou[1], Liang Dai[1], Wenchao Shen[1], Jun Zheng[1,2], Yan Ma[1,2], Mindong Chen[1,2]

1. School of Environmental Science and Engineering, Nanjing University of Information Science and Technology, Nanjing, China

2. Collaborative Innovation Center of Atmospheric Environment and Equipment Technology, Nanjing University of Information Science and Technology, Nanjing, China

Corresponding authors: hyu@nuist.edu.cn

Abstract

Particle size distribution down to 1.4 nm was measured in the urban atmosphere of Nanjing, China in spring, summer and winter during 2014-2015. Sub-3 nm particle event, which is equivalent to nucleation event, occurred on 42 out of total 90 observation days, but new particles could grow to cloud condensation nuclei (CCN)-active sizes on only 9 days. In summer, infrequent nucleation was limited by both unfavorable meteorological conditions (high temperature and RH) and reduced anthropogenic precursor availability due to strict emission control measures during the 2014 Youth Olympic Games in Nanjing. The limiting factors for nucleation in winter and spring were meteorological conditions (radiation, temperature, and RH) and condensation sink, but for the further

growth of sub-3 nm particles to CCN-active sizes, anthropogenic precursors again became limiting factors. Nucleation events were strong in the polluted urban atmosphere. Initial $J_{1.4}$ at the onset and peak $J_{1.4}$ at the noontime could be up to 2.1×10^{2} cm^{-3} s^{-1} and 2.5×10^{3} cm^{-3} s^{-1}, respectively, during the 8 nucleation events selected from different seasons. Time-dependent $J_{1.4}$ usually showed good linear correlations with a sulfuric acid proxy for every single event (R^2 = 0.56 - 0.86, excluding a day with significant nocturnal nucleation), but the correlation among all the 8 events deteriorated (R^2 = 0.17) due to temperature or season change. We observed that new particle growth rate did not increase monotonically with particle size, but had a local maximum up to 25 nm h^{-1} between 1-3 nm. The growth rate behavior was interpreted in this study as the solvation effect of organic activating vapor in newly formed inorganic nuclei.

1. Introduction

New particle formation (NPF) is an important source of secondary aerosols in the atmosphere (Kulmala et al., 2004a). Field studies and model simulations have consistently shown that NPF can enhance cloud condensation nuclei (CCN) concentrations and contribute significantly to the global CCN production (Wiedensohler et al., 2009; Yue et al., 2011; Spracklen et al., 2008; Pierce and Adams, 2009; Merikanto, 2009; Yu and Luo, 2009; Matsui et al. 2013). NPF is a two-stage process consisting of formation of clusters and subsequent growth to detectable sizes (Kulmala et al., 2000). Recently, chamber experiments have made substantial progress in revealing the fundamental processes involved in particle nucleation and growth (Kirkby et al., 2011; Almeida et al., 2013; Schobesberger et al., 2013; Riccobono et al., 2014; Ehn et al., 2014; Kürten et al., 2014). However,

consistent theories are still under investigation to quantify the processes physically, chemically, and dynamically (Kulmala et al., 2013, 2014). For example, the identity and physico-chemical properties of assisting vapors other than sulfuric acid (H_2SO_4) are uncertain so far. It is also uncertain what mechanisms allow the assisting vapors to overcome strong Kelvin effect over sub-3 nm particles. Existing mechanisms include condensation of extremely low volatility organic compounds (Ehn et al., 2014), nano-Köhler activation (Kulmala et al., 2004b), heterogeneous chemical reactions (Zhang and Wexler, 2002), heterogeneous nucleation (Wang et al., 2013), and adsorption of organics on cluster surface (Wang and Wexler, 2013). However, the relative importance of various mechanisms is unknown.

Direct measurements of size- and time dependent nucleation rate and growth rate in sub-3 nm size range are important to constrain the relative contributions from different mechanisms and precursors. Such measurements are also important to evaluate the survival probability of new particle to CCN-active sizes (~100 nm for soluble particles at 0.2% super saturation, Pierce and Adams, 2009) and to reveal the limiting factors in the process. Recently, a series of new instruments have been developed to measure sub-3 nm aerosol number concentration and chemical composition, such as condensation particle counters (e.g., PSM, DEG-SMPS, Jiang et al., 2011a; Sipila et al., 2009; Vanhanen et al., 2011), ion spectrometers (e.g., NAIS, Asmi et al., 2009), and mass spectrometers (e.g., Cluster-CIMS, APi-TOF, CI-APi-TOF, Jokinen et al., 2012; Junninen et al., 2010; Zhao et al., 2010). Kuang et al. (2012) developed a de-coupling method to measure size- and time dependent growth rates of sub-5 nm particles. Their results at two urban sites in U.S.A showed that size-resolved growth rates increased approximately linearly with particle size from 1 to 5 nm.

Similar results were also observed in the Boreal forest (Kulmala et al., 2013; Lehtipalo et al., 2014). Based on growth rates measured below 2 nm, Kulmala et al. (2013) identified three separate size regimes, which were dominated by different key gas to particle conversion processes.

The relative contribution of different precursors and mechanisms to the nucleation and growth of 1-3 nm particles may vary greatly with atmospheric conditions (Riipinen et al., 2012). Therefore, sub-3 nm particle measurements in a variety of atmospheric conditions, e.g., remote or urban atmosphere, biogenic- or anthropogenic emission dominated areas, are immensely valuable. Unfortunately, such data are very sparse until now (Jiang et al., 2011b; Kuang et al., 2012; Kulmala et al., 2013; Lehtipalo et al., 2009, 2010, 2011; Yu et al., 2014a, b). China is suffering from severe atmospheric particulate matter pollution in recent years (Chan and Yao, 2008; Yue et al., 2011). To the best of our knowledge, only two studies were conducted in China to measure the occurrence of new particles down to ~1 nm. In these two studies, air ions (Herrmann et al., 2014) or neutral particles (Xiao et al., 2015) were measured by AIS or PSM in two urban locations of Yangtze River Delta region. Both studies were conducted in the winter season.

Here we reported the nucleation and growth of sub-3 nm particles in the urban atmosphere of Nanjing, China on arbitrarily selected observation days in spring, summer and winter of 2014-2015. Our aim was to (1) provide new information about the initial steps of NPF based on size- and time resolved nucleation rate and growth rate measurements, and (2) find possible limiting factors behind the seasonal and diurnal variations of nucleation events in the polluted urban atmosphere.

2. Methodology

2.1 Field measurements

Nanjing is the second largest megacity after Shanghai in the Yangtze River Delta (YRD) region of China (Chan and Yao, 2008). The YRD city cluster, covering 2.1 $\times 10^5$ km^2 land with 170 million residents, is one of the most populated and industrialized regions in China. Field measurement was conducted from the third floor (15m above the ground level) of an academic building beside a Chinese national meteorology observatory facility in NUIST campus (32.20^o N, 118.71^o E, symbol ① in Figure 1). The sampling was carried out during the months of May (May 10-30, 2014), June (June 1-15, 2014), December (December 24-31, 2014), February (February 16-22, 2015), and March (March 1-7, 2015). Total 58 measurement days were arbitrarily selected to represent spring, early summer and winter seasons, but to avoid any rain-event.

As part of an intensive summer campaign (12 August-12 September 2014), the summer measurement was conducted at a local governmental meteorology observatory platform (32.06^{o}N, 118.70^{o}E) that is 14km south to the NUIST site (② in Figure 1). The instruments were housed in an air conditioned trailer, using exactly the same sampling inlets as the NUIST site. The main aim of the summer campaign was to understand the effects of regional emission control measures during the 2014 Young Olympic Games (August 1-September 15) on air quality. Because the two sites locate within the same urban air shed, the measurement provided an opportunity to study seasonal variation of nucleation and its relationship with meteorological variables and gaseous precursors.

Sub-3 nm clusters/particles (hereafter referred as particles) were measured with a nano condensation nucleus counter system (nCNC) consisting of a Particle Size Magnifier (PSM model A10, Airmodus Oy, Finland) and a butanol Condensation Particle Counter (model A20, Airmodus Oy, Finland). During the measurement, an ambient air flow of 14 standard liters per minute (slpm)

was drawn into building room or trailer via a 72 cm long and 1.0 cm I.D diameter stainless steel (SS) tube, which was extended outside the room/trailer horizontally. PSM then sampled a split flow of 2.5 slpm via a SS T-union. The design of the inlet tubing (length and air flow rate) was to minimize the transport loss of nano particles. The size dependent transport survival ratios of sub-3 nm particles in the inlet tubing was estimated (67 %-86 % for 1.4-3.0 nm) and corrected using a particle loss calculator tool (von der Weiden et al., 2009).

PSM was operated in a continuous scanning mode with a cycle of 240 steps between saturator flow rates of 0.1 and 1.0 slpm within 240 seconds. The particle cut-off sizes of the nCNC varied with saturation ratios in the saturator (Vanhanen et al., 2011). A step-wise method was used to invert raw scanning data to size spectrum (time resolution: 4 minutes) of sub-3 nm particles, which were classified evenly into 6 size bins, i.e. 1.4-1.6, 1.6-1.9, 1.9-2.2, 2.2-2.4, 2.4-2.7, and 2.7-3.0 nm. The inverted particle number concentrations in the 6 bins were referred as $N_{1.5}$, $N_{1.8}$, $N_{2.0}$, $N_{2.3}$, $N_{2.6}$ and $N_{2.8}$, using mean values of upper and lower size boundaries in each bin. The step-wise method was described in detail by Lehtipalo et al. (2014).

Particle size distributions in the range from 3 - 750 nm were obtained by integrating two scanning mobility particle spectrometers (SMPS) with a nano-SMPS (a TSI differential mobility analyzer DMA3085 and a condensation particle counter CPC3776; scanning range: 3 - 64 nm) and a long-SMPS (TSI DMA3081 and CPC3775; scanning range: 64 - 750 nm). During the summer campaign, only the long-SMPS was operated to scan particles from 8 - 350 nm. Scanning cycles of both SMPS systems were 4 minutes, in order to synchronize with the nCNC. The SMPSs sampled ambient air from a separate sampling inlet. The inlet was a 129 cm long and 1.0 cm I.D

125 horizontally-oriented SS tube with an air flow of 14 slpm. The transport loss of particles in the SMPS
126 inlets was corrected using size dependent survival ratios of 85-100% for particles > 3 nm.

127 Sulfur dioxide (SO_2), ozone (O_3), carbon monoxide (CO) and nitrogen oxides (NO and NO_2)
128 concentrations were measured every 1 minute with Thermo Environmental Instruments (model
129 43i-TLE, 49i, 48i, and 42i, respectively). When gaseous SO_2, O_3, NO_2 and CO data were not
130 available, hourly SO_2, O_3, NO_2 and CO were obtained from nearby local Environmental Protection
131 Agency (EPA) monitoring station. $PM_{2.5}$ was monitored with Thermo Scientific TEOM 1405.
132 Meteorological variables including wind speed, wind direction, relative humidity (RH), temperature
133 and solar radiation flux were recorded every 1 hour during the measurement periods. Mean
134 concentrations of $PM_{2.5}$, SO_2, and O_3 were 79 $\mu g\ m^{-3}$, 10 ppbv and 48 ppbv, respective, during the
135 whole measurement period. Therefore, we regard our measurement environment as a polluted urban
136 atmosphere.

137

138 **2.2 Nucleation event and growth patterns**

139 A criterion was set to determine whether the nCNC detected sub-3nm particles in the atmosphere.
140 The criterion was that total particle concentration reading followed the supersaturation scanning
141 cycle of PSM so that the highest concentrations were measured at lowest cut-off sizes (see also
142 Figure 2 in Lehtipalo et al., 2014). However, it was possible in the step-wise inversion method that
143 the number concentration fluctuation of > 3 nm particles within a 4-min scanning cycle was wrongly
144 inverted to sub-3 nm particles even when sub-3 nm particles actually did not exist according to the
145 above criterion. As a result, the step-wise inversion method always reported a background sub-3 nm

particle concentration ($N_{sub\text{-}3}$, i.e. the sum of $N_{1.5}$, $N_{1.8}$, $N_{2.0}$, $N_{2.3}$, $N_{2.6}$ and $N_{2.8}$) of 0.5×10^3 - 2×10^3 cm^{-3} in the nighttime and 3×10^3 - 8×10^3 cm^{-3} in the daytime. Similar background levels of sub-3 nm particles during non-NPF periods were also reported by other studies that used the nCNC (Kulmala et al., 2013; Lehtipalo et al., 2014; Xiao et al., 2015). Following their procedures, we did not attempt to subtract this background from $N_{sub\text{-}3}$ reported in this study.

We defined sub-3 nm particle event as sub-3 nm particle occurrence with $N_{sub\text{-}3}$ higher than background level persisting for longer than 1 h in the atmosphere. In this study, we used sub-3 nm particle event as an approximate measure of nucleation event. This is because (1) there was an approximately positive linear correlation between $N_{sub\text{-}3}$ and nucleation rate ($J_{1.4}$ in this study, see next section) with R^2 of 0.94 (Figure 2), and (2) $N_{sub\text{-}3}$ calculation needs only nCNC scanning data and was thus more readily available than $J_{1.4}$ calculation which needs both nCNC and SMPS scanning data. Similar definition has been discussed in our previous studies (Yu et al., 2014a, b). Apparently, a sub-3 nm particle event did not necessarily lead to an NPF event always, but it indicated the intensity and frequency of nucleation in the atmosphere. One focus in this work was to investigate the characteristics of sub-3 nm particle event.

Particle growth after nucleation is crucial to determine if nucleated particles could grow to CCN-active sizes. We identified two growth patterns according to size spectrum characteristics in sub-3 nm size range (Figure 3). In a Type A event (Figure 3a or b), size distribution n(D_p, t) was higher at smaller sizes (e.g., 1.4–1.6 nm) than n(D_p, t) at larger sizes (e.g., 2.7–3.0 nm). The size spectrum below 3 nm thus looked like a "volcano". In a Type B event (Figure 3c or d), n(D_p, t) was lower at smaller sizes than n(D_p, t) at larger sizes ("up-side-down volcano"). For the size range > 3

nm, depending on whether a banana-shape growth was seen, we further defined Type A1/A2 and Type B1/B2 events: particles eventually grew to CCN-active sizes in Type A1 and B1 events, while in Type A2 and B2 events banana-shape particle growth to CCN-active sizes was not seen. Therefore, Type A1 and B1 events were equivalent to conventional NPF events based on either DMPS or SMPS measurements.

Type B size distribution was more unusual since n(D_p, t) of small particles were less than n(D_p, t) of large particles in the sub-3 nm size range. We excluded the possibility of deteriorated nCNC detection efficiencies for small particles due to high particle loading in the sample air. This is because total number concentrations of nCNC during our measurements never approached nCNC upper concentration limit 4×10^5 cm^{-3}, especially in the early stage of nucleation when total particle concentration was rather low. Our nCNC was also calibrated periodically using H_2SO_4-H_2O particles in a laboratory flow tube to ensure the detection efficiency of the nCNC. The different chemical composition of atmospheric particles could be another factor of lower detection efficiencies. It is well known that organic substances activate less readily in diethylene glycol (e.g. Kangasluoma et al. 2014). However, it is accepted in general that larger particles have higher mass fraction of organics than smaller particles in a NPF process. If organic substances activate less readily in DEG, it should be even more difficult to activate larger particles than smaller particles. Therefore, the increasing n(D_p) with D_p (i.e. upside down volcano) could not be simply due to lower detection efficiency of organic substances.

2.3 Formation rate and growth rate calculations with a simplified GDE method

187 Conventional appearance time method determined growth rates (hereafter, *GR*) during the initial
188 period of NPF by finding the time steps when newly-formed particles appeared at certain size bins
189 and calculating the *GR* from the time differences between successive size bins (Kulmala et al., 2012;
190 Lehtipalo et al., 2014). This method was often not applicable to the NPF event with high *GR* below 3
191 nm, e.g., 0.3 nm/4 min (i.e. 4.5 nm h^{-1}) with size intervals 0.3 nm and scanning time intervals 4
192 minutes in our measurements. Furthermore, sub-3 nm particles were often generated persistently
193 throughout the daytime period. Maximum concentrations in the sub-3 nm size bins could appear
194 around noontime, which is a few hours later than the onset of nucleation. Therefore, we were not
195 able to pinpoint correctly maximum or 50% maximum concentrations at the onset of nucleation.

196 The rapid growth of small particles in the urban atmosphere was the motivation that we used an
197 alternative method to calculate growth rate and formation rate. Here, we analyzed 8 events (listed in
198 Table 1, including both Type A1/A2 and B1/B2 events) in detail, for which complete size spectra
199 from 1.4 - 750 nm were available without distorted, broken or noisy data. Total 8 size bins were
200 classified: 6 evenly-divided size bins in sub-3 nm and 2 size bins in 3-30 nm (3-10 and 10-30 nm).
201 For an aerosol population that is growing through simultaneous condensation and coagulation,
202 aerosol general dynamic equation (GDE) describes the evolution of number concentration in a size
203 bin between particle diameters D_{p1} and D_{p2} ($D_{p2} > D_{p1}$) as:

204 $$\frac{\mathrm{d}N(D_{p1},D_{p2},\mathrm{t})}{\mathrm{dt}} = J(D_{p1},\mathrm{t}) - J(D_{p2},\mathrm{t}) - \mathrm{CoagSnk}(D_{p1},D_{p2},\mathrm{t}) + \mathrm{CoagSrc}(D_{p1},D_{p2},\mathrm{t}) \quad (1)$$

205

where $N(D_{p1}, D_{p2}, \mathrm{t})$ is the number concentration from D_{p1} to D_{p2}, inverted from nCNC or SMPS scanning data. J is condensational growth flux (i.e. particle formation rate) across the lower ($D_{p,1}$) or upper ($D_{p,2}$) boundaries of a size bin. In the first size bin of 1.4-1.6 nm, $J(1.4\ \mathrm{nm}, \mathrm{t})$, or simply $J_{1.4}$, is the unknown formation rate of the smallest particles that we measured.

$\mathrm{CoagSnk}(\mathrm{D_{p1}}, \mathrm{D_{p2}}, \mathrm{t})$ and $\mathrm{CoagSrc}(\mathrm{D_{p1}}, \mathrm{D_{p2}}, \mathrm{t})$ are the sink and source terms defining the coagulation out of and into the size bin between D_{p1} and D_{p2}. Assuming bin k has lower boundary $D_{p,1}$ and upper boundary $D_{p,2}$,

$$\mathrm{CoagSnk}(\mathrm{D_{p1}}, \mathrm{D_{p2}}, \mathrm{t}) = \mathrm{N(k,t)} \sum_{\mathrm{i=1}}^{98} (1 - \theta_{\mathrm{k,i,k}}) \mathrm{K_{k,i}}\ \mathrm{N(i,t)} \quad (2)$$

$$\mathrm{CoagSrc}(\mathrm{D_{p1}}, \mathrm{D_{p2}}, \mathrm{t}) = \frac{1}{2} \sum_{\mathrm{i=1}}^{\mathrm{k-1}} \sum_{\mathrm{j=1}}^{\mathrm{k-1}} \theta_{\mathrm{i,j,k}}\ \mathrm{K_{i,j}} \mathrm{N(j,t)} \mathrm{N(i,t)} \quad (3)$$

Here $\mathrm{N(i,t)}$ is number concentration of bin i. $\mathrm{K_{i,j}}$ is coagulation kernel for a collision between particles from bins i and j. Probability coefficient $\theta_{\mathrm{i,j,k}} = 1$, if the volume sum of two coagulating particles ($\mathrm{v_i} + \mathrm{v_j}$, here the volume is calculated from the center diameter of a bin) is within the volume boundaries of bin k. otherwise $\theta_{\mathrm{i,j,k}} = 0$. The particle coagulation of total 98 bins was considered, but the coagulation terms were only needed to be calculated for the smallest 8 bins from 1.4 to 30 nm. According to our calculation, $\mathrm{CoagSrc}(\mathrm{D_{p1}}, \mathrm{D_{p2}}, \mathrm{t})$ accounted for only 0 - 0.8 % of the total particle flux into a bin (i.e. $\mathrm{CoagSrc}(\mathrm{D_{p1}}, \mathrm{D_{p2}}, \mathrm{t}) + J(D_{p1}, \mathrm{t})$) in the sub-3 nm size range. This implied that self coagulation played a negligible role and most of the production flux into a bin is due to condensational growth from gas molecules.

The GDE here is the same as the Eq. 1 by Kuang et al. (2012). In their method, gaseous H_2SO_4 was measured simultaneously and a constant $GR(D_p, \mathrm{t}) / GR_{H2SO4}(D_p, \mathrm{t})$ ratio at a given size over time

was assumed. Their $GR(D_p, \mathrm{t})$ was then solved by fitting the GDE to the measured size distributions. In our study, however, we did not measure gaseous H_2SO_4. Instead, $J(30\ \mathrm{nm}, \mathrm{t})$ in the largest size bin, which is the condensational growth flux out of 30 nm, was set to zero. This simplification was valid in the four Type A2/B2 events when particles never grew to > 30 nm (March 4, February 19, May 20 and May 16). In the rest four Type A1/B1 events (February 18, December 27, May 15, and August 15), this was also valid during the early NPF period when particles did not grow out of 30 nm and during the late NPF period when particles grew out of 30 nm completely. During the middle period of events (usually around 11:00 AM-14:00 PM), $J(30\ \mathrm{nm}, \mathrm{t})$ was underestimated and thus $J_{1.4}$ could be regarded as a lower estimate. In the four Type A2/B2 events, our calculation showed that J_{10} was only 0-4% of $J_{1.4}$. Xiao et al. (2015) and Kulmala et al. (2013) measured both $J_{1.5}$ and J_3 using appearance time method. Their J_3 was less than 7% of $J_{1.5}$. Furthermore, $J_{30}/J_{1.4}$ ratio should be even smaller than $J_{10}/J_{1.4}$ or $J_3/J_{1.5}$ ratios, considering the 8 events were carefully selected to ensure all sub-30 nm particles were grown from nucleation (not emitted directly from emission sources like vehicular engine). All these evidences supported that even if J_{30} was set to 0, $J_{1.4}$ would not be underestimated more than 7% when particles grew cross 30 nm on February 18, December 27, May 15, and August 15.

Equation 1 requires the balance of condensational growth (J), coagulation terms (CoagSnk and CoagSrc) and the changing rate of particle number concentration (dN/dt). Using Eq. (1) we can therefore calculate the nucleation rate $J(1.4\ \mathrm{nm}, \mathrm{t})$ and formation rates $J(D_p, \mathrm{t})$ across all size bin boundaries from 1.6 to 10 nm. After the formation rates $J(D_p, \mathrm{t})$ were obtained, $GR(D_p, \mathrm{t})$ was calculated from $J(D_p, \mathrm{t})/\mathrm{n}(D_p, \mathrm{t})$, where $\mathrm{n}(D_p, \mathrm{t})$ is size distribution calculated as $\mathrm{n}(D_p, \mathrm{t}) = \frac{\mathrm{d}N(\mathrm{t})}{\mathrm{d}D_p}$

247 for each size bin. On the other hand, the appearance time method could still be applied to (1) the size
248 range of > 3 nm where size intervals were large (2-6 nm), and (2) the size range of < 3 nm when *GR*
249 was small. The results from appearance time method will also be showed in the next section.

250

251 **3. Results and discussion**

252 Section 3.1, sections 3.2-3.4 and section 3.5 were organized, respectively, to address the
253 following 3 issues: (1) seasonal variation, diurnal variation and limiting factors of nucleation event
254 (represented by sub-3 nm particle event) in the polluted urban atmosphere, (2) time- and size
255 dependent nucleation rate and growth rate of sub-3 nm particles, and their implications for nucleation
256 and growth mechanisms, (3) Inhibited particle growth to CCN-active sizes in strong nucleation
257 events of Type B2.

258 **3.1 Seasonal and diurnal variations of nucleation event**

259 As seen from Figure 2, there was an approximate linear correlation between $N_{sub\text{-}3}$ and $J_{1.4}$ with
260 the slope of $N_{sub-3}/J_{1.4}$ equal to ~160. This seemed to suggest that the average residence time of
261 new particles in the sub-3 nm size range was 160 seconds before they were scavenged due to
262 coagulation or grew out of 3 nm. The sub-3 nm particles observed at the present work were thus
263 formed in situ in the urban atmosphere and not likely to be carried-over by air transport. In this
264 section we used sub-3 nm particle event as an approximate measure of nucleation.

265 We observed significant seasonal characteristics of nucleation event (Figure 4). Nucleation was
266 rare and weak in summer, while it was commonly observed in all other seasons. During our

measurements from 2014 to 2015, nucleation events occurred on 81% of all spring observation days (May 2014), 53% in early summer (June 2014), 10% in summer (August and September 2014), and 64% in winter (December 2014, February and March 2015). We compared intensity ($N_{sub\text{-}3}$) and frequency of nucleation events, as well as meteorological variables (temperature, RH, wind speed, and solar radiation flux) and gaseous pollutants (SO_2, NO_2, CO and O_3) for spring, summer and winter seasons. June was not shown in Figure 4 for comparison, because it was a transit season from spring (May) to summer (August and September). The data were first averaged over the entire event period for each event; and we then used event-averaged data to create box and whistler plots for the 3 seasons. $PM_{2.5}$ was used here as a surrogate of condensational sink (*CS*), because of the more ready availability of $PM_{2.5}$ data than SMPS data.

As shown in Figure 4, nucleation in summer was characterized by lowest frequency, lowest $N_{sub\text{-}3}$ (2.2×10^4 cm^{-3}), and short nucleation period (only 1-2 hours). Strict emission control measures during the 2014 Youth Olympic Games resulted in relatively low $PM_{2.5}$ level (32 ± 8 μ g m^{-3}), which should favor nucleation. However, relatively low SO_2 concentration (1.4 ± 0.6 ppbv), high temperature (26 ± 2 ^oC), and high RH (74.3 ± 4.2 %) might not be in favor of nucleation. A simple H_2SO_4 proxy (Radiation $\times SO_2/PM_{2.5}$) indicated that summer H_2SO_4 concentration was likely to be the lowest among the 3 seasons, which could explain low nucleation intensity/frequency.

We further examined diurnal variations of $N_{sub\text{-}3}$ and other variables on event and non-event days in winter (Figure 5). Because nucleation in winter was characterized by Type B event ("up-side-down volcano" below 3 nm), event days were further divided to Type B1 and Type B2 events depending on whether banana-shape particle growth was seen. The difference between Type

B1 and B2 will be discussed later in Section 3.5. During the non-event days, $N_{sub\text{-}3}$ ranged from 2.4×10^3 cm^{-3} in the night to 8.0×10^3 in the day, which was close to background levels. During the event days, $N_{sub\text{-}3}$ in the night was close to that of non-event days, but could reach 8×10^4 - 20×10^4 cm^{-3} in the middle of the day. This was more than 10 times higher than those on the non-event days. From Figure 5 we can see that non-event day had higher concentrations of anthropogenic precursors (indicated by SO_2, NO_2, and CO), but nucleation seemed to be limited by higher pre-existing particle surface area (indicated by $PM_{2.5}$), higher temperature and RH, and lower radiation flux. Photochemistry indicators O_3 was also lower during non-event days.

Nucleation in spring was characterized by highest frequency (81%) among all seasons. Highest gaseous pollutant concentration of (H_2SO_4 proxy, SO_2, NO_2, CO and O_3) and radiation seemed to the favorable factors to explain this. However, $N_{sub\text{-}3}$ in spring (3.3×10^4 cm^{-3}) was much lower than that in winter (11.2×10^4 cm^{-3}). Unfavorable factors included high pre-existing particle surface area ($PM_{2.5}$: 112 ± 68 $\mu g\ m^{-3}$) and high temperature (27 ± 4 ^oC) in spring. Integrating the above seasonal and diurnal variation information in Figure 4 and Figure 5, we tentatively identified that the limiting factors for nucleation in our urban atmosphere were (1) radiation, temperature, RH and *CS* in winter and spring, and (2) temperature, RH and available gaseous precursors in summer.

Out of total 90 measurement days, March 4, 2015 in winter was the only day that we observed significant nocturnal nucleation. Sunrise and sunset were at 6:29 AM and 18:00 PM local time on March 4, but nucleation were observed persistently from 4:00 AM - 20:00 PM. $N_{sub\text{-}3}$ increased from 3.5×10^3 cm^{-3} at 4:00 AM to 6.3×10^4 cm^{-3} before sunrise. During 10:00-11:00 AM, peak $N_{sub\text{-}3}$ reached 3×10^4 cm^{-3}, 3 times higher than the average of all other event days in winter. Apparently,

309 nocturnal nucleation on March 4 could not be explained as carry-over of daytime particles nor being
310 associated with photochemistry. This implied the existence of certain dark nucleation source. There
311 are a number of observations that have also shown nighttime particle formation events in various
312 atmospheric conditions (Junninen et al., 2008; Lehtipalo et al., 2011; Lee et al., 2008; Ortega et al.,
313 2009, 2012; Russell et al., 2007; Suni et al., 2008; Svenningsson et al., 2008; Yu et al., 2014), but the
314 mechanisms behind the nocturnal nucleation are yet still highly speculative. With our instrument
315 capability in this work, we could not deduce any valuable information on the nocturnal nucleation
316 mechanism, except that we found the air mass on 04 March was relatively clean (both *CS* and gases,
317 mean *CS*: 0.15 s^{-1}), and temperature and RH (mean: 4.4^{o}C and 33%) were favorable for nucleation.

318

319 **3.2 Size- and time dependent formation rates of sub-3 nm particles**

320 We observed 23 Type A events and 9 Type B events during the measurements. The different
321 size distribution patterns (Figure 3) were probably linked to the mechanism or intensity of nucleation
322 and growth. To address this issue, we first compared the formation rates and growth rates in two
323 types of events. Formation rates *J* of 1.4, 1.6, 1.9, 2.2, 2.4, 2.7 and 3.0 nm particles were shown in
324 Figure 6 (upper panels) for typical Type A and Type B events. It is obvious that $J_{1.4}$ was much higher
325 on February 18 (Type B) than that on May 15 (Type A). A clear time dependence of *J* was observed.
326 For example, $J_{1.4}$ was 60 cm^{-3} s^{-1} at the onset of the nucleation event on May 15 and increased to 300
327 $cm^{-3}s^{-1}$ in the middle of the day. In the type B event on February 19, the initial and peak $J_{1.4}$ were
328 2.1×10^{2} and 1.2×10^{3} $cm^{-3}s^{-1}$ respectively. Therefore, our method provided more information of
329 nucleation than conventional calculation methods that usually showed only an averaged *J* at the onset

of a nucleation event. Our method was also different from Kulmala et al. (2013). Their time-dependent formation rate on an event day was equal to size distribution n(D_p,t) times a constant growth rate at the onset of the event obtained with the appearance time method.

The diurnal variation of *J* implied that nucleation was probably linked to sunlight induced photochemistry. We calculated the correlations between $J_{1.4}$ and an H_2SO_4 proxy for the 8 events of our interest. The H_2SO_4 proxy was calculated following $[H_2SO_4] = 8.21 \times 10^{-3} k \cdot Radiation \cdot [SO_2]^{0.62} \cdot (CS \cdot RH)^{-0.13}$(Eq. 8 of Mikkonen et al. 2011), where k is the temperature-dependent reaction-rate constant. Figure 7a show that good linear correlation was usually seen for every single event with R^2 ranging from 0.72 to 0.86 for 6 out of 8 events. A moderate R^2 of 0.56 was obtained for August 15. R^2 was lowest (0.34) on March 4, 2015. This is not surprising because we know March 4 was the only day with nocturnal nucleation during the measurement period. The H_2SO_4 proxy was also calculated using the derivation of Petäjä et al. (2009), which resulted in lower R^2 of log $J_{1.4}$ *vs.* log $[H_2SO_4]$ for all 8 events. Therefore, in this study we used Mikkonen H_2SO_4 proxy, as it was derived with more comprehensive datasets than Petäjä et al. (2009). The slopes of log $J_{1.4}$ *vs.* log $[H_2SO_4]$ were close to 1 in all events (0.82-1.17, excluding March 4), indicating activation theory can explain the nucleation mechanism in our urban atmosphere.

If data points of all the 8 events were put together, the linear correlation between H_2SO_4 proxy and $J_{1.4}$ deteriorated (slope=1.1, R^2=0.17, Figure 7b). In spite of considerable scattering, most of data points located between $J_{1.4}=10^{-4.1} \times [H_2SO_4]$ and $J_{1.4}=10^{-6.3} \times [H_2SO_4]$. An interesting finding was that the scattering of $J_{1.4}$ *vs.* $[H_2SO_4]$ proxy among all 8 events was probably due to temperature or season change (Figure 7b). More specifically, with the same level of H_2SO_4 proxy, $J_{1.4}$ was higher in

351 winter with lower temperature than in spring/summer with higher temperature. There were two
352 possibilities behind the deteriorated linear correlation between H_2SO_4 proxy and $J_{1.4}$: (1) inaccurate
353 H_2SO_4 proxy and (2) other varying factors in nucleation mechanism. First, it was very likely that
354 H_2SO_4 concentrations in our polluted urban atmosphere were overestimated by the H_2SO_4 proxy of
355 Mikkonen et al. (2011), which was based on statistic regression of historical datasets from relatively
356 clean Europe/USA atmosphere. The extent of overestimation may vary with the levels of predictor
357 variables (e.g., SO_2, temperature, *CS*). Mean SO_2 mixing ratios were 10.5 and 7.3 ppbv in
358 spring/summer and winter during our measurements, respectively. These were 1 order of magnitude
359 higher than SO_2 mixing ratios at the 6 European and USA sites (mean values: 0.23-3.4 ppbv,
360 Mikkonen et al., 2011). Our *CS* in the 8 events was on the order of magnitude of 10^{-2} s^{-1}, again higher
361 than 10^{-3} s^{-1} in Mikkonen et al. (2011). Mikkonen et al. (2011) had already pointed out that the
362 predictive ability was lower for long term data due to atmospheric condition changes in different
363 seasons.

364 Second, organic condensing vapor concentrations in particle growth events were higher in winter
365 than those in spring/summer (Table 1, see Section 3.4). If the organics were also involved in
366 nucleation, $J_{1.4}$ should be enhanced in winter. The enhancement of nucleation by organics (most
367 likely anthropogenic organics in our urban atmosphere) could be supported by the comparison of $J_{1.4}$
368 dependences on H_2SO_4 between our study and the measurements in the Boreal forest: besides
369 possible H_2SO_4 overestimation, $J_{1.4}=10^{-4.1}\times[H_2SO_4] - 10^{-6.3}\times[H_2SO_4]$ in our sites was much higher
370 than $J_{1.5}=1.06\times10^{-7}[H_2SO_4]^{1.1}$ in Hyytiälä during active aerosol formation periods (Kulmala et al.,

2013). At last, low temperature itself might enhance nucleation in winter (Brus et al., 2011) via increasing the saturation ratios of all nucleation precursors (e.g., water, H_2SO_4, organics).

3.3 Size- and time dependent growth rates of sub-3 nm particles

Particle size distribution n(D_p) and corresponding GR(D_p) at an instant in time during the events were shown in Figure 6 middle and lower panels. A local minimum of n(D_p) at 2.4 nm, followed by a local maximum somewhere between 2.5 and 10 nm, was seen on May 15, 2014. Such size distribution characteristics on May 15, 2014, as well as on all other Type A event days, was also observed by Kulmala et al. (2013) in the Boreal forest (Figure 1A and S9A in their paper) and by Jiang et al. (2011b) in the urban area of Atlanta, USA (Figure 1 in their paper). We further examined the growth rates in the size range of 1-3 nm on May 15, 2014. It was shown that there was a local maximum of GR(D_p) at 2.4 nm. This could explain why n(D_p) was increasing in 2.4-3 nm size range: when particle condensational flow out of a size bin was slowed down, it was possible that particles flowing into the size bin accumulated, leading to particle number increase in the bin.

We saw more unusual behaviors of n(D_p) and GR(D_p) in the Type B event on February 18 (Figure 6 right panels): GR(D_p) decreased monotonically in the size range of 1.4 - 3 nm, and accordingly n(D_p) increased monotonically at the same time. A high GR(D_p) of 25 nm h^{-1} was observed at 1.6 nm and GR(D_p) decreased rapidly to 1.7 nm h^{-1} at ~3 nm. If we consider that GR(D_p) below 1.6 nm would eventually decrease due to strong Kelvin effect of all possible precursors (H_2SO_4 or organics), the overall trend of GR(D_p) in the Type B event was in fact the same as Type A:

391 for the smallest clusters, growth rate was small (possibly below 1 nm h^{-1}) and increased with D_p. It
392 reached a local maximum somewhere between 1-3 nm, after which $GR(D_p)$ decreased with D_p. For a
393 typical NPF event, $GR(D_p)$ would eventually increase again after a local minimum between 3-10 nm.
394 The difference between the Type A event (February 18) and Type B event (May 15) was the D_p of
395 local maximum $GR(D_p)$ (2.4 nm *vs.* 1.6 nm).

396 The interesting behaviors of $n(D_p)$ and GR (D_p) in our urban atmosphere were different from the
397 stereotyped understanding that steady-state cluster size distribution $n(D_p)$ decreases with D_p in
398 nucleation and GR increases monotonically with D_p in an NPF event. It should be pointed out that if
399 we calculated the overall GR in 1.4-3 nm, $GR_{1.4\text{-}3}$ was 3.6 nm h^{-1} on May 15 and 4.4 nm h^{-1} on
400 February 18, which were still smaller than $GR_{3\text{-}20}$ during the initial period of the events (7.7 and 6.0
401 nm h^{-1}, calculated using appearance time method). Table 1 showed that a faster $GR_{3\text{-}20}$ than $GR_{1.4\text{-}3}$
402 were quite common, except in two events on May 16 and 20 when particles did not grow beyond 3
403 nm. Overall, GR was still increasing with increasing D_p.

404 Kuang et al. (2012) had also reported a local maximum of GR at ~2.6 nm in an NPF event
405 measured in Atlanta, USA (Figure 1b in their paper). In this study we further point out that GR could
406 decrease monotonically with D_p in 1-3 nm range in strong nucleation events. Our GR was calculated
407 from a simplified GDE method, however, the decease of GR in 1-3 nm size range could be easily
408 inferred from the size spectra shown in Figure 3 or Figure 6 middle panels: for a D_{p2} that was larger
409 than D_{p1}, particle formation rate $J(D_{p2})$ must be smaller than $J(D_{p1})$. If we observed a higher $n(D_{p2})$
410 than $n(D_{p1})$, $GR(D_p)$ that was equal to $J(D_p)/n(D_p)$ must be smaller at D_{p2} than D_{p1}.

411 Apparently, the complicated growth rate behaviors in our polluted urban atmosphere can not be
412 explained by H_2SO_4 condensation alone, not only because H_2SO_4 condensational growth rate
413 (GR_{H2SO4}, calculated from the H_2SO_4 proxy and shown as black dashed lines in Figure 6) was smaller
414 than the measured growth rate ($GR_{measured}$), but also because GR_{H2SO4} curve should follow a
415 monotonically decreasing trend in > 1 nm sizes assuming a collision-only condensational growth
416 without vaporization (Nieminen et al., 2010).

417

418 **3.4 Growth rate due to activating vapor on newly formed nuclei in sub-3 nm sizes**

419 Nano-Köhler theory (Anttila et al., 2004; Kulmala et al., 2004b, c) suggested that when a soluble
420 organic vapor is dissolved in newly formed nuclei of aqueous-phase sulfate at certain size between
421 1-3 nm, the surface organic vapor pressure is lowered and thus assists the growth of the nuclei. Here,
422 we continued our discussion based on the nano-Köhler theory to provide an explanation of *GR*
423 behaviours observed in our urban atmosphere. The net uptake of gaseous molecules by a
424 nanoparticle is driven by the difference of the condensational flux (governed by gas-phase
425 concentration far from the particle C_∞) and the evaporation flux (governed by equilibrium surface
426 concentration over the nuclei $C_{surface}$). $C_{surface}$ was determined by the pure component saturation
427 vapor pressure C^*, particle curvature $\exp\left(\frac{4\sigma v}{kTD_p}\right)$ and particle composition. The growth rate due to
428 the uptake of an activating organic vapor (hereafter, denoted as ELVOC, extremely low volatility
429 organic compound) was expressed as

430 $$GR_{ELVOC} = \frac{\gamma}{2\rho_v}\left(1+\frac{D_v}{D_p}\right)^2\left(\frac{8kT}{\pi}\right)^{\frac{1}{2}}\left(\frac{1}{m_p}+\frac{1}{m_v}\right)^{\frac{1}{2}} m_v(C_\infty - C_{surface}) \quad (4)$$

where $C_{surface} = C^* \exp\left(\frac{4\sigma v}{kTD_p}\right)(x_{D_p} + \exp(-\varphi(D_p/D_{p0})^3))$.

The kinetic prefactor $\frac{\gamma}{2\rho_v}\left(1+\frac{D_v}{D_p}\right)^2\left(\frac{8kT}{\pi}\right)^{\frac{1}{2}}\left(\frac{1}{m_p}+\frac{1}{m_v}\right)^{\frac{1}{2}} m_v$ was taken from Nieminen et al. (2010). x_{D_p} is the mole fraction of water-soluble ELVOC in the pseudobinary solution consisting of ELVOC and the aqueous sulfate nuclei. An example of x_{D_p} as a function of D_p was shown in Figure 8a. Nuclei activation diameter $D_{p,act}$ is the size that ELVOC begins to dilute the nuclei. Before activation ($D_p < D_{p,act}$), organic fraction in the particle does not increase significantly. As a result of strong Kelvin effect, $C_{surface}$ increases with decreasing D_p (Figure 8b dashed black line). A fixed organic fraction of 5% is plotted in the Figure 8a and 8b, for simplification, for the particle before activation. The actual organic fraction in such small particles before activation is unknown and most likely to vary. Therefore, in Eq. (4) an empirical term $\exp(-\varphi(D_p/D_{p0})^3)$ was added to account for the rapidly decreasing $C_{surface}$ in the size range of $D_p < D_{p,act}$. Here, D_{p0} is 1 nm to cancel off the unit of D_p. When $D_p \rightarrow 0$, the term $x_{D_p} + \exp(-\varphi(D_p/D_{p0})^3) \rightarrow 1$.

For $D_p > D_{p,act}$, the empirical term $\exp(-\varphi(D_p/D_{p0})^3) \rightarrow 0$. Consequently, $C_{surface}$ for $D_p > D_{p,act}$ is in effect equal to $C^* \exp\left(\frac{4\sigma v}{kTD_p}\right) x_{D_p}$. Because $D_{p,act}$ is the size that ELVOC begins to dilute the nuclei, the rapidly increasing organic fraction in the small size regime of 2-3 nm raises the equilibrium $C_{surface}$ of ELVOC first. Then after the particle is dominated by organics in 3-6 nm, $C_{surface}$ decreases to merge with the Kelvin curve of a pure organic droplet (red line, Figure 8b). $C_{surface}$ for $D_p > D_{p,act}$ (solid black line, Figure 8b) is thus the same as the nano Köhler curve in Figure 1 of Kulmala et al. 2004b. The pseudobinary solution was treated ideal here in the Eq. (4).

The complete equilibrium curve of $C_{surface}$ in 1-6 nm (dashed + solid black lines) was shown in Figure 8c. The blue line represented the calculated $C_\infty - C_{surface}$. The trend of $C_\infty - C_{surface}$ coincided with the size dependence of the measured *GR* (*GR*$_{measure}$). *D*$_{p,act}$ corresponded to the size with local maximum *GR*$_{measure}$. We fitted GR_{ELVOC} with *GR*$_{measure}$ in sub-3 nm sizes at an instant in time by adjusting 3 free parameters in Eq. (4): C^*, C_∞, and φ. Other parameters like surface tension (0.02 N m^{-1}) and molar volume (135.5 cm^3 mol^{-1}) of ELVOC were taken from Kulmala et al. (2004b). Molecule diameter d_v (0.8 nm) and condensed-phase density ρ_v (1.5 g cm^{-3}) of ELVOC were taken from Ehn et al. (2014). Uptake coefficientγ was calculated following Nieminen et al. (2010). The fitting results in Figure 9 showed that the dependence of *GR*$_{GDE\ method}$ on *D*$_p$ below 3 nm could be well reproduced by Eq. (4) for both Type A and Type B events. Free parameter φ determined the slope of the dashed black line in Figure 8b. φ was fitted to be 0.4-1.0 for the 8 events. C_∞ determined the local maximum *GR* at the *D*$_{p,act}$. C_∞ and C^* determined the local minimum *GR* at the right side of *D*$_{p,act}$. Therefore, C^* and C_∞ shown in Table 1 were basically determined by the measured *GR* (local maximum and local minimum) and not sensitive to φ. As shown in Table 1, the activating vapor concentrations C_∞ were $2.3\times10^7 - 2.0\times10^8$ cm^{-3}. The saturation vapor concentration C^* were 2.5×10^6-5.7×10^7 cm^{-3}. They were within the orders of magnitude of 10^7-10^8 cm^{-3} and 10^6-10^7 cm^{-3} suggested by Kulmala et al. (2004b), respectively.

For comparison, the *GR* calculated from appearance time method was also shown in Figure 9 (*GR*$_{AT\ method}$) for > 3 nm particles on May 15, February 18 and February 19, as well as for sub-3 nm particles on May 20 when particle growth was relatively slow. It can be seen that the *GR* on May 20 calculated from the two methods agreed well with each other, leading credit to our GDE method.

$GR_{AT\ method}$ in >10 nm sizes was usually underestimated by GR_{ELVOC}. This could be interpreted as other condensing vapors with higher volatility may contribute to particle growth in the larger particles. It should be noted that the appearance time method followed the time steps when newly-formed particles appeared in successive size bins and thus $GR_{AT\ method}$ was not the growth rates at the same instant in time.

For all the 8 nucleation events, Table 1 summarizes the measured values of overall growth rate in 1.4-3 nm ($GR_{1.4\text{-}3}$), maximum growth rate in 1.4-3 nm ($GR_{max,1.4\text{-}3}$), overall growth rate in 3-20 nm ($GR_{3\text{-}20}$), nucleation rate ($J_{1.4}$), activation diameter ($D_{p,act}$), *CS*, and temperature (*T*) during the event periods with maximum nucleation rates. Corresponding estimates of Mikkonen H_2SO_4 proxy, C_∞ and C^* were shown in the right 3 columns. It can be seen that in comparison with more conventional Type A events, Type B events usually occurred with (1) higher $J_{1.4}$, $GR_{max,1.4\text{-}3}$, $GR_{1.4\text{-}3}$, C_∞, and *CS*; (2) smaller $D_{p,act}$; and (3) lower *T*. However, the H_2SO_4 proxy and $GR_{3\text{-}20}$ were similar in Type A and Type B events. Based on these estimations, we concluded that higher ELVOC concentration C_∞ was the key factor leading to the higher $J_{1.4}$ and $GR_{1.4\text{-}3}$, which in turn resulted in the different size spectrum pattern in Type B events ("up-side-down volcano") from in Type A events ("volcano").

It should be noted that the organic vapor concentrations C_∞ referred to in this study were not directly measured, but estimated based on Eq. (4). Aerosol dynamic processes, such as nucleation, coagulation, and the condensation growth of H_2SO_4 and water vapors, were not considered explicitly in Eq. (4). In addition, bulk thermodynamics was applied in Eq. (4) for extremely small clusters/particles of sub-3 nm sizes. Therefore, although our calculation provided an possibility to

492 explain the size dependence of growth rate observed in the polluted urban atmosphere, C_∞ in this
493 study was subject to uncertainties in (1) the growth rate derived from the GDE method, (2) the theory
494 by which the growth rate was related to the organic vapor concentration, and (3) H_2SO_4 level which
495 also contributed to the initial growth.

496

497 **3.5 Inhibited particle growth to CCN-active sizes in strong nucleation events of Type B2**

498 Type B2 was strong nucleation event that produced rather high concentrations of new particles
499 in sub-20 nm size range (Figure 3d). High concentrations of activating vapor in these events (e.g.,
500 C_∞: 1.4-2.0 $\times 10^8$ cm^{-3} on February 18 and March 4) should favor a banana-shape NPF event with fast
501 growth of particles >20 nm, due to weakened Kelvin effect. However, it was puzzling to us why new
502 particles accumulated in 2-20 nm and did not grow further on Type B2 event days (see Figure 3d).
503 We first examined the air mass trajectory characteristics of Type B2 events. Compared with Type B1,
504 Type B2 was characterized by long range transport air masses from far north of China and Mongolia.
505 The lumped trajectories with insignificant wind direction change imply that the air mass in Type B2
506 event was quite uniform. In addition, meteorological and chemical variables (high solar radiation
507 flux and wind speed, low temperature, $PM_{2.5}$, SO_2, NO_2, CO and O_3, green lines in Figure 5)
508 collectively suggested that Type B2 was typical regional event in homogeneous cold air masses.
509 Therefore, the interrupted growth of new particles was not likely to be a result of wind direction
510 change.

As seen from Figure 5, meteorological variables on Type B2 days were generally more favorable in aiding particle growth than on Type B1 days: lower $PM_{2.5}$, lower temperature, and higher solar radiation flux. The unfavorable factors in Type B2 events, however, included lower concentrations of SO_2, NO_2, and CO (anthropogenic emission indicators), lower secondary photochemical product indicators O_3 and lower particle phase sulfate in 100-1000 nm (X. Ge, private communication, 2015, X. Ge conducted simultaneous AMS measurement during our measurement periods). All these evidences suggested that further particle growth in Type B2 events was limited by certain condensing vapor other than ELVOC. Consequently, although there was a pool of sub-20 nm particles, they were not further "activated" due to the low availability of this condensing vapor. Following the terminology of Donahue et al. (2011, 2012), we called this condensing vapor LVOC (low volatility organic compounds)

The above hypothesis was sound if we considered that the identity of LVOC for the growth of particles > 20 nm could be different from ELVOC for sub-3 nm particle growth. Hirsikko et al. (2005) observed that $GR_{3\text{-}20}$ demonstrated an opposite seasonal cycle to $GR_{1.3\text{-}3}$: $GR_{3\text{-}20}$ was higher in summer, whereas $GR_{1.3\text{-}3}$ was higher in winter. This suggested that the condensing vapors were different in identity for particles of different sizes. Hirsikko et al. (2005) attributed the condensing vapors for $GR_{3\text{-}20}$ to biogenetic VOCs. In our urban atmosphere, according to Figure 5, LVOC was more likely to be from anthropogenic sources associated with SO_2, NO_x and CO emissions. A picture of the growth process was thus like this: ELVOC of lower volatility, lower concentration and higher water solubility activated inorganic nuclei and accelerated particle growth in smaller sizes. This in turn assisted in the condensation of LVOC of high volatility, low solubility, but with larger amount

of mass. The further growth of particles >20 nm, which means significant increment of particle mass, needed continuous supply of LVOC from the anthropogenic sources. On the Type B2 days, LVOC supply was not adequate (low SO_2, CO and NO_x). As a result, continuous banana-shape particle growth did not take place.

4. Conclusion

NPF can contribute to CCN only after going through nucleation, initial growth steps and subsequent growth to CCN-active sizes. This study provided the evidences of limiting factors in these processes in a polluted urban atmosphere in China. We observed atmospheric nucleation events on 42 out of total 90 observation days, but particles could grow to CCN-active sizes on only 9 days, which was equivalent to 9 conventional NPF events. In summer, strict emission control measures during the 2014 Youth Olympic Games resulted in relatively low $PM_{2.5}$ and anthropogenic trace gases (SO_2, NO_2, CO and O_3) levels. Infrequent nucleation was thus limited by both low concentrations of gaseous precursors and high temperature and RH in summer. In more polluted winter and spring atmosphere, precursor supply was not limiting anymore; nucleation occurred once meteorological conditions were favorable (i.e. low *CS* and temperature/RH, higher solar radiation). However, for the further growth of sub-3 nm particles to CCN-active sizes, anthropogenic gaseous precursors again became limiting factors.

A simplified GDE method was used in this study to calculate particle formation rates first and then growth rates. Nucleation events were strong in the polluted urban atmosphere of Nanjing. Initial $J_{1.4}$ at the onset and peak $J_{1.4}$ at the noontime could be up to 2.1×10^2 cm^{-3} s^{-1} and 2.5×10^3 cm^{-3} s^{-1}, respectively, during the 8 nucleation events selected from different seasons. The diurnal variation of

553 $J_{1.4}$ implied that nucleation was usually linked to sunlight induced photochemistry. Time-dependent
554 $J_{1.4}$ showed good linear correlations with the H_2SO_4 proxy for every single event, except a day with
555 significant nocturnal nucleation. However, the correlation between $J_{1.4}$ and the H_2SO_4 proxy for all 8
556 events deteriorated, which might reflect the effect of temperature or assisting vapor concentration in
557 the nucleation. The deteriorated correlation could also be due to the lower predictive ability of the
558 H_2SO_4 proxy in the polluted urban atmosphere for different seasons.

559 In all nucleation events, a local maximum growth rate was observed between 1-3 nm with *GR* up
560 to 25 nm h^{-1}. This means *GR* was not monotonically increasing with particle size. The overall $GR_{1.4\text{-}3}$,
561 however, was still smaller than $GR_{3\text{-}20}$, if particles could grow beyond 3 nm. The local maximum
562 growth rate was interpreted as the solvation effect of organic activating vapor in newly formed
563 inorganic nuclei. Based on our estimation, high ELVOC concentration of 2.3×10^7 - 2.0×10^8 cm^{-3} was
564 expected to be the key factor leading to high $GR_{1.4\text{-}3}$. The varying *GR* of new particle in turn resulted
565 in the different particle growth patterns that we observed in Nanjing.

566 Our results call for a more robust proxy of gaseous H2SO4 to be developed for polluted urban
567 conditions. The study also highlighted the importance of estimating or measuring activating organic
568 vapor levels (using CI-APi-TOF, for example) in the initial growth steps of atmospheric NPF. Our
569 year-round measurement data provided valuable size evolution data of sub-3 nm clusters/particles to
570 evaluate previous aerosol dynamic models of new particle formation. A robust dynamic model was
571 needed to appropriately treat all aerosol and gas-phase processes in the initial growth steps.

572

573 **Acknowledgements**

574 This work was supported by National Science Foundation of China (41405116,
575 41275142, 41575122), Natural Science Foundation of Jiangsu Province (BK20140989), and Jiangsu
576 Specially Appointed Professor grant. The measurement campaigns were partially funded by the
577 Priority Academic Program Development of Jiangsu Higher Education Institutions (PAPD). We
578 thank Dr. Vijay P. Kanawade and Dr. Xinlei Ge for valuable discussion.

579

580 **References:**

581 Almeida, J., Schobesberger, S., Kurten, A., Ortega, I. K., Kupiainen-Maatta, O., Praplan, A. P.,
582 Adamov, A., Amorim, A., Bianchi, F., Breitenlechner, M., David, A., Dommen, J., Donahue, N.
583 M., Downard, A., Dunne, E., Duplissy, J., Ehrhart, S., Flagan, R. C., Franchin, A., Guida, R.,
584 Hakala, J., Hansel, A., Heinritzi, M., Henschel, H., Jokinen, T., Junninen, H., Kajos, M.,
585 Kangasluoma, J., Keskinen, H., Kupc, A., Kurten, T., Kvashin, A. N., Laaksonen, A., Lehtipalo,
586 K., Leiminger, M., Leppa, J., Loukonen, V., Makhmutov, V., Mathot, S., McGrath, M. J.,
587 Nieminen, T., Olenius, T., Onnela, A., Petaja, T., Riccobono, F., Riipinen, I., Rissanen, M.,
588 Rondo, L., Ruuskanen, T., Santos, F. D., Sarnela, N., Schallhart, S., Schnitzhofer, R., Seinfeld, J.
589 H., Simon, M., Sipila, M., Stozhkov, Y., Stratmann, F., Tome, A., Trostl, J., Tsagkogeorgas, G.,
590 Vaattovaara, P., Viisanen, Y., Virtanen, A., Vrtala, A., Wagner, P. E., Weingartner, E., Wex, H.,
591 Williamson, C., Wimmer, D., Ye, P., Yli-Juuti, T., Carslaw, K. S., Kulmala, M., Curtius, J.,
592 Baltensperger, U., Worsnop, D. R., Vehkamaki, H., and Kirkby, J.: Molecular understanding of

593 sulphuric acid-amine particle nucleation in the atmosphere, Nature, 502(7471), 359-363,
594 doi:10.1038/nature12663, 2013.

595 Anttila, T., Kerminen, V. M., Kulmala, M., Laaksonen, A., and O'Dowd, C. D.: Modelling the
596 formation of organic particles in the atmosphere, Atmos. Chem. Phys., 4(4), 1071-1083, doi:
597 10.5194/acp-4-1071-2004, 2004.

598 Asmi, E., Sipilä, M., Manninen, H. E., Vanhanen, J., Lehtipalo, K., Gagné, S., Neitola, K., Mirme,
599 A., Mirme, S., Tamm, E., Uin, J., Komsaare, K., Attoui, M., and Kulmala, M.: Results of the first
600 air ion spectrometer calibration and intercomparison workshop, Atmos. Chem. Phys., 9(1),
601 141-154, doi: 10.5194/acp-9-141-2009, 2009.

602 Brus, D., Neitola, K., Hyvärinen, A.-P., Petäjä, T., Vanhanen, J., Sipilä, M., Paasonen, P., Kulmala,
603 M., and Lihavainen, H.: Homogenous nucleation of sulfuric acid and water at close to
604 atmospherically relevant conditions, Atmos. Chem. Phys., 11(11), 5277-5287, doi:
605 10.5194/acp-11-5277-2011, 2011.

606 Chan, C. K., and Yao, X.: Air pollution in mega cities in China, Atmos. Environ., 42(1), 1-42,
607 doi: :10.1016/j.atmosenv.2007.09.003.

608 Donahue, N. M., Trump, E. R., Pierce, J. R., and Riipinen, I.: Theoretical constraints on pure
609 vapor-pressure driven condensation of organics to ultrafine particles, Geophys. Res. Lett., 38(16),
610 L16801, doi: 10.1029/2011gl048115, 2011.

611 Donahue, N. M., Kroll, J. H., Pandis, S. N., and Robinson, A. L.: A two-dimensional volatility basis
612 set – Part 2: Diagnostics of organic-aerosol evolution, Atmos. Chem. Phys., 12(2), 615-634, doi:
613 10.5194/acp-12-615-2012, 2012.

614 Ehn, M., Thornton, J. A., Kleist, E., Sipila, M., Junninen, H., Pullinen, I., Springer, M., Rubach, F.,
615 Tillmann, R., Lee, B., Lopez-Hilfiker, F., Andres, S., Acir, I.-H., Rissanen, M., Jokinen, T.,
616 Schobesberger, S., Kangasluoma, J., Kontkanen, J., Nieminen, T., Kurten, T., Nielsen, L. B.,
617 Jorgensen, S., Kjaergaard, H. G., Canagaratna, M., Maso, M. D., Berndt, T., Petaja, T., Wahner,
618 A., Kerminen, V. M., Kulmala, M., Worsnop, D. R., Wildt, J., and Mentel, T. F.: A large source
619 of low-volatility secondary organic aerosol, Nature, 506(7489), 476-479, doi:
620 10.1038/nature13032, 2014.

621 Herrmann, E., Ding, A. J., Kerminen, V.-M., Petäjä, T., Yang, X. Q., Sun, J. N., Qi, X. M.,
622 Manninen, H., Hakala, J., Nieminen, T., Aalto, P. P., Kulmala, M., and Fu, C. B.:: Aerosols and
623 nucleation in eastern China: first insights from the new SORPES-NJU station, Atmos. Chem.
624 Phys., 14, 2169-2183, doi: 10.5194/acp-14-2169-2014, 2014.

625 Hirsikko, A., Laakso, L., Horrak, U., Aalto, P. P., Kerminen, V. M., and Kulmala, M.: Annual and
626 size dependent variation of growth rates and ion concentrations in boreal forest, Boreal Environ.
627 Res., 10, 357-469, 2005.

628 Jiang, J., Chen, M., Kuang, C., Attoui, M., and McMurry, P. H.: Electrical Mobility Spectrometer
629 Using a Diethylene Glycol Condensation Particle Counter for Measurement of Aerosol Size

630 Distributions Down to 1 nm, Aerosol Sci. Technol., 45(4), 510-521, doi:
631 10.1080/02786826.2010.547538, 2011a.

632 Jiang, J., Zhao, J., Chen, M., Eisele, F. L., Scheckman, J., Williams, B. J., Kuang, C., and McMurry,
633 P. H.: First Measurements of Neutral Atmospheric Cluster and 1-2 nm Particle Number Size
634 Distributions During Nucleation Events, Aerosol Sci. Technol., 45(4), II-V, doi:
635 10.1080/02786826.2010.546817, 2011b.

636 Jokinen, T., Sipilä, M., Junninen, H., Ehn, M., Lönn, G., Hakala, J., Petäjä, T., Mauldin III, R. L.,
637 Kulmala, M., and Worsnop, D. R.: Atmospheric sulphuric acid and neutral cluster measurements
638 using CI-APi-TOF, Atmos. Chem. Phys., 12(9), 4117-4125, doi: 10.5194/acp-12-4117-2012,
639 2012.

640 Junninen, H., Hulkkonen, M., Riipinen, I., Nieminen, T., Hirsikko, A., Suni, T., Boy, M., Lee, S.-H.,
641 Vana, M., Tammet, T., Kerminen, V. M., and Kulmala, M.: Observations on nocturnal growth of
642 atmospheric clusters, Tellus Ser. B, 60, 365-371, doi:10.1111/j.1600-0889.2008.00356.x, 2008.

643 Junninen, H., Ehn, M., Petäjä, T., Luosujärvi, L., Kotiaho, T., Kostiainen, R., Rohner, U., Gonin, M.,
644 Fuhrer, K., Kulmala, M., and Worsnop, D. R.: A high-resolution mass spectrometer to measure
645 atmospheric ion composition, Atmos. Meas. Tech., 3, 1039-1053, doi: 10.5194/amtd-3-599-2010,
646 2010.

647 Kangasluoma, J., Kuang, C., Wimmer, D., Rissanen, M. P., Lehtipalo, K., Ehn, M., Worsnop, D.R.,
648 Wang, J., Kulmala, M. and Petäjä, T.: Sub-3 nm particle size and composition dependent

649 response of a nano-CPC battery. Atmos. Meas. Tech., 7, 689-700, doi: 10.5194/amt-7-689-2014,
650 2014.

651 Kirkby, J., Curtius, J., Almeida, J., Dunne, E., Duplissy, J., Ehrhart, S., Franchin, A., Gagne, S.,
652 Ickes, L., Kurten, A., Kupc, A., Metzger, A., Riccobono, F., Rondo, L., Schobesberger, S.,
653 Tsagkogeorgas, G., Wimmer, D., Amorim, A., Bianchi, F., Breitenlechner, M., David, A.,
654 Dommen, J., Downard, A., Ehn, M., Flagan, R. C., Haider, S., Hansel, A., Hauser, D., Jud, W.,
655 Junninen, H., Kreissl, F., Kvashin, A., Laaksonen, A., Lehtipalo, K., Lima, J., Lovejoy, E. R.,
656 Makhmutov, V., Mathot, S., Mikkila, J., Minginette, P., Mogo, S., Nieminen, T., Onnela, A.,
657 Pereira, P., Petaja, T., Schnitzhofer, R., Seinfeld, J. H., Sipila, M., Stozhkov, Y., Stratmann, F.,
658 Tome, A., Vanhanen, J., Viisanen, Y., Vrtala, A., Wagner, P. E., Walther, H., Weingartner, E.,
659 Wex, H., Winkler, P. M., Carslaw, K. S., Worsnop, D. R., Baltensperger, U., and Kulmala, M.:
660 Role of sulphuric acid, ammonia and galactic cosmic rays in atmospheric aerosol nucleation,
661 Nature, 476(7361), 429-433, doi:10.1038/nature10343, 2011.

662 Kuang, C., Chen, M., Zhao, J., Smith, J., McMurry, P. H., and Wang, J.: Size- and time-resolvedt
663 growth rate measurements of 1 to 5 nm freshly formed atmospheric nuclei, Atmos. Chem. Phys.,
664 12(9), 3573-3589, doi: 10.5194/acpd-11-25427-2011, 2012.

665 Kulmala, M., Pirjola, L., and Makela, J. M.: Stable sulfate clusters as a source of new atmospheric
666 particles, Nature, 404, 60-66, doi: 10.1038/35003550, 2000.

667 Kulmala, M., Laakso, L., Lehtinen, K. E. J., Riipinen, I., Dal Maso, M., Lauria, A., Kerminen, V. M.,
668 Birmili, W., McMurry, P.H.: Formation and growth rates of ultrafine atmosphere particles: A
669 review of observations, J. Aerosol. Sci., 35, 143-176, 2004a.

670 Kulmala, M., Kerminen, V. M., Anntila, T., Laaksonen, A., and O'Dowd, C. D.: Organic aerosol
671 formation via sulfate cluster activation, J. Geophys. Res., 109, D04205, doi:
672 10.1029/2003JD003961, 2004b.

673 Kulmala, M., Laakso, L., Lehtinen, K. E. J., Riipinen, I., Dal Maso, M., Anttila, T., Kerminen, V.-M.,
674 Hõrrak, U., Vana, M., and Tammet, H.: Initial steps of aerosol growth, Atmos. Chem. Phys.,
675 4(11), 2553-2560, doi: 10.5194/acp-4-2553-2004, 2004c.

676 Kulmala, M., Petäjä, T., Nieminen, T., Sipilä, M., Manninen, H. E., Lehtipalo, K., Dal Maso, M.,
677 Aalto, P. P., Junninen, H., Paasonen, P., Riipinen, I., Lehtinen, K. E. J., Laaksonen, A., and
678 Kerminen, V. M.: Measurement of the nucleation of atmospheric aerosol particles, Nat. Protocols,
679 7(9), 1651-1667, doi: 10.1038/nprot.2012.091, 2012.

680 Kulmala, M., Kontkanen, J., Junninen, H., Lehtipalo, K., Manninen, H. E., Nieminen, T., Petäjä, T.,
681 Sipilä, M., Schobesberger, S., Rantala, P., Franchin, A., Jokinen, T., Järvinen, E., Äijälä, M.,
682 Kangasluoma, J., Hakala, J., Aalto, P. P., Paasonen, P., Mikkilä, J., Vanhanen, J., Aalto, J.,
683 Hakola, H., Makkonen, U., Ruuskanen, T., Mauldin, R. L., Duplissy, J., Vehkamäki, H., Bäck, J.,
684 Kortelainen, A., Riipinen, I., Kurtén, T., Johnston, M. V., Smith, J. N., Ehn, M., Mentel, T. F.,
685 Lehtinen, K. E. J., Laaksonen, A., Kerminen, V. M., and Worsnop, D. R.: Direct Observations of

686 Atmospheric Aerosol Nucleation, Science, 339(6122), 943-946, doi: 10.1126/science.1227385,
687 2013.

688 Kulmala, M., Petäjä, T., Ehn, M., Thornton, J., Sipilä, M., Worsnop, D. R. and Kerminen, V. M.:
689 Chemistry of Atmospheric Nucleation: On the Recent Advances on Precursor Characterization
690 and Atmospheric Cluster Composition in Connection with Atmospheric New Particle Formation,
691 Annu. Rev. Phys. Chem., 65, 21–37, doi: 10.1146/annurev-physchem-040412-110014, 2014.

692 Kürten, A., Jokinen, T., Simon, M., Sipilä, M., Sarnela, N., Junninen, H., Adamov, A., Almeida, J.,
693 Amorim, A., Bianchi, F., Breitenlechner, M., Dommen, J., Donahue, N. M., Duplissy, J., Ehrhart,
694 S., Flagan, R. C., Franchin, A., Hakala, J., Hansel, A., Heinritzi, M., Hutterli, M., Kangasluoma,
695 J., Kirkby, J., Laaksonen, A., Lehtipalo, K., Leiminger, M., Makhmutov, V., Mathot, S., Onnela,
696 A., Petäjä, T., Praplan, A. P., Riccobono, F., Rissanen, M. P., Rondo, L., Schobesberger, S.,
697 Seinfeld, J. H., Steiner, G., Tomé, A., Tröstl, J., Winkler, P. M., Williamson, C., Wimmer, D., Ye,
698 P., Baltensperger, U., Carslaw, K. S., Kulmala, M., Worsnop, D. R., and Curtius, J.: Neutral
699 molecular cluster formation of sulfuric acid–dimethylamine observed in real time under
700 atmospheric conditions, Proc. Natl. Acad. Sci. U.S.A., 111(42), 15019-15024,
701 doi:10.1073/pnas.1404853111, 2014.

702 Lee, S. H., Young, L. H., Benson, D. R., Kulmala, M., Junninen, H., Suni, T., Campos, T., Rogers, D.
703 C., and Jensen, J.: Observations of nighttime new particle formation in the troposphere, J.
704 Geophys. Res., 113, D10210, doi: 10210.11029/12007JD009351, 2008.

705 Lehtipalo, K., Sipilä, M., Riipinen, I., Nieminen, T., and Kulmala, M.: Analysis of atmospheric
706 neutral and charged molecular clusters in boreal forest using pulse-height CPC, Atmos. Chem.
707 Phys., 9, 4177–4184, 2009.

708 Lehtipalo, K., Sipila, M., Junninen, H., Ehn, M., Berndt, T., Kajos, M. K., Worsnop, D. R., Petaja, T.,
709 and Kulmala, M.: Nanoparticles in boreal forest and coastal environment: a comparison of
710 observations and implications of the nucleation mechanism, Atmos. Chem. Phys., 10, 7009-7016,
711 2010.

712 Lehtipalo, K., Sipila, M., Junninen, H., Ehn, M., Berndt, T., Kajos, M. K., Worsnop, D. R., Petaja, T.,
713 and Kulmala, M.: Observations of Nano-CN in the Nocturnal Boreal Forest, Aerosol Sci.
714 Technol., 45(4), 499-509, doi: 10.1080/02786826.2010.547537, 2011.

715 Lehtipalo., K., Leppä, J., Kontkanen., J., Kangasluoma., J., Franchin., A., Wimmer., D.,
716 Schobesberger., S., Junninen., H., Petäjä, T., Sipilä, M., Mikkilä, J., Vanhanen., J., Worsnop., D.
717 R., and Kulmala, M.: Methods for determining particle size distribution and growth rates between
718 1 and 3 nm using the Particle Size Magnifier, Boreal Environ. Res., 19, 215–236, 2014.

719 Matsui, H., Koike, M., Takegawa, N., Kondo, Y., Takami, A., Takamura, T., Yoon, S., Kim, S. W.,
720 Lim, H. C., and Fast, J. D.: Spatial and temporal variations of new particle formation in East Asia
721 using an NPF-explicit WRF-chem model: North-south contrast in new particle formation
722 frequency, J. Geophys. Res., 118(20), 11,647-611,663, doi:10.1002/jgrd.50821, 2013.

723 Merikanto, J., Spracklen, D. V., Mann, G. W., Pickering, S. J., and Carslaw, K. S.: Impact of
724 nucleation on global CCN, Atmos. Chem. Phys., doi: 10.5194/acp-9-8601-2009, 9, 8601-8616,
725 2009.

726 Mikkonen, S., Romakkaniemi, S., Smith, J. N., Korhonen, H., Petäjä, T., Plass-Duelmer, C., Boy, M.,
727 McMurry, P. H., Lehtinen, K. E. J., Joutsensaari, J., Hamed, A., Mauldin III, R. L., Birmili, W.,
728 Spindler, G., Arnold, F., Kulmala, M., and Laaksonen, A.: A statistical proxy for sulphuric acid
729 concentration, Atmos. Chem. Phys., 11:11319-11334, doi: 10.5194/acpd-11-20141-2011, 2011.

730 Nieminen, T., Lehtinen, K. E. J., and Kulmala, M.: Sub-10 nm particle growth by vapor
731 condensation - effects of vapor molecule size and particle thermal speed, Atmos. Chem. Phys.,
732 10(20), 9773-9779, doi: 10.5194/acp-10-9773-2010, 2010.

733 Ortega, I. K., Suni, T., Gronholm, T., Boy, M., Hakola, H., Hellen, H., Valmari, T., Arvela, H.,
734 Vehkamaki, H., and Kulmala, M.: Is eucalyptol the cause of nocturnal events observed in
735 Australia?, Boreal Environ. Res., 14(4), 606-615, 2009.

736 Ortega, I. K., Suni, T., Boy, M., Grönholm, T., Manninen, H. E., Nieminen, T., Ehn, M., Junninen,
737 H., Hakola, H., Hellén, H., Valmari, T., Arvela, H., Zegelin, S., Hughes, D., Kitchen, M., Cleugh,
738 H., Worsnop, D. R., Kulmala, M., and Kerminen, V. M.: New insights into nocturnal nucleation,
739 Atmos. Chem. Phys., 12(9), 4297-4312, doi:10.5194/acp-12-4297-2012, 2012.

740 Petäjä, T., Mauldin, III, R. L., Kosciuch, E., McGrath, J., Nieminen, T., Paasonen, P., Boy, M.,
741 Adamov, A., Kotiaho, T., and Kulmala, M.: Sulfuric acid and OH concentrations in a boreal
742 forest site, Atmos. Chem. Phys., 9, 7435–7448, doi:10.5194/acp-9-7435-2009, 2009.

743 Pierce, J. R., and Adams, P. J.: Uncertainty in global CCN concentrations from uncertain aerosol
744 nucleation and primary emission rates, Atmos. Chem. Phys., 9(4), 1339-1356, doi:
745 10.5194/acp-9-1339-2009, 2009.

746 Riccobono, F., Schobesberger, S., Scott, C. E., Dommen, J., Ortega, I. K., Rondo, L., Almeida, J.,
747 Amorim, A., Bianchi, F., Breitenlechner, M., David, A., Downard, A., Dunne, E. M., Duplissy, J.,
748 Ehrhart, S., Flagan, R. C., Franchin, A., Hansel, A., Junninen, H., Kajos, M., Keskinen, H., Kupc,
749 A., Kürten, A., Kvashin, A. N., Laaksonen, A., Lehtipalo, K., Makhmutov, V., Mathot, S.,
750 Nieminen, T., Onnela, A., Petäjä, T., Praplan, A. P., Santos, F. D., Schallhart, S., Seinfeld, J. H.,
751 Sipilä, M., Spracklen, D. V., Stozhkov, Y., Stratmann, F., Tomé, A., Tsagkogeorgas, G.,
752 Vaattovaara, P., Viisanen, Y., Vrtala, A., Wagner, P. E., Weingartner, E., Wex, H., Wimmer, D.,
753 Carslaw, K. S., Curtius, J., Donahue, N. M., Kirkby, J., Kulmala, M., Worsnop, D. R., and
754 Baltensperger, U.: Oxidation Products of Biogenic Emissions Contribute to Nucleation of
755 Atmospheric Particles, Science, 344(6185), 717-721, doi:10.1126/science.1243527, 2014.

756 Riipinen, I., Yli-Juuti, T., Pierce, J. R., Petaja, T., Worsnop, D. R., Kulmala, M., and Donahue, N.
757 M.: The contribution of organics to atmospheric nanoparticle growth, Nature Geosci., 5(7),
758 453-458, doi: 10.1038/NGEO1499, 2012.

759 Russell, L. M., Mensah, A. A., Fischer, E. V., Sive, B. C., Varner, R. K., Keene, W. C., Stutz, J., and
760 Pszenny, A. A. P.: Nanoparticle growth following photochemical α- and β-pinene oxidation at
761 Appledore Island during International Consortium for Research on Transport and
762 Transformation/Chemistry of Halogens at the Isles of Shoals 2004, J. Geophys. Res., 112(D10),
763 D10S21, doi:10.1029/2006jd007736, 2007.Seinfeld, J. H., and Pandis, S. N.: Atmospheric

764 chemistry and physics: from air pollution to climate change, 2nd ed., John Wiley and Sons. Inc.,
765 New York, 2006.

766 Schobesberger, S., Junninen, H., Bianchi, F., Lönn, G., Ehn, M., Lehtipalo, K., Dommen, J., Ehrhart,
767 S., Ortega, I. K., Franchin, A., Nieminen, T., Riccobono, F., Hutterli, M., Duplissy, J., Almeida,
768 J., Amorim, A., Breitenlechner, M., Downard, A. J., Dunne, E. M., Flagan, R. C., Kajos, M.,
769 Keskinen, H., Kirkby, J., Kupc, A., Kürten, A., Kurtén, T., Laaksonen, A., Mathot, S., Onnela, A.,
770 Praplan, A. P., Rondo, L., Santos, F. D., Schallhart, S., Schnitzhofer, R., Sipilä, M., Tomé, A.,
771 Tsagkogeorgas, G., Vehkamäki, H., Wimmer, D., Baltensperger, U., Carslaw, K. S., Curtius, J.,
772 Hansel, A., Petäjä, T., Kulmala, M., Donahue, N. M., and Worsnop, D. R.: Molecular
773 understanding of atmospheric particle formation from sulfuric acid and large oxidized organic
774 molecules, Proc. Natl. Acad. Sci. U.S.A., doi:10.1073/pnas.1306973110, 2013.

775 Sipila, M., Lehtipalo, K., Attoui, M., Neitola, K., Petäjä, T., Aalto, P. P., O'Dowd, C. D., and
776 Kulmala, M.: Laboratory Verification of PH-CPC's Ability to Monitor Atmospheric Sub-3 nm
777 Clusters, Aerosol Sci. Technol., 43(2), 126-135, doi: 10.1080/02786820802506227, 2009.

778 Spracklen, D. V., Carslaw, K. S., Kulmala, M., Kerminen, V.-M., Sihto, S.-L., Riipinen, I.,
779 Merikanto, J., Mann, G. W., Chipperfield, M. P., Wiedensohler, A., Birmili, W., and Lihavainen,
780 H.: Contribution of particle formation to global cloud condensation nuclei concentrations,
781 Geophys. Res. Lett., 35(6), L06808, doi:10.1029/2007GL033038, 2008.

782 Suni, T., Kulmala, M., Hirsikko, A., Bergman, T., Laakso, L., Aalto, P. P., Leuning, R., Cleugh, H.,
783 Zegelin, S., Hughes, D., van Gorsel, E., Kitchen, M., Vana, M., Hõrrak, U., Mirme, S., Mirme, A.,

784 Sevanto, S., Twining, J., and Tadros, C.: Formation and characteristics of ions and charged
785 aerosol particles in a native Australian Eucalypt forest, Atmos. Chem. Phys., 8(1), 129-139,
786 doi:10.5194/acp-8-129-2008, 2008.

787 Svenningsson, B., Arneth, A., Hayward, S., Holst, T., Massling, A., Swietlicko, E., Hirsikko, A.,
788 Junninen, H., Riipinen, I., Vana, M., Dal Maso, M., Hussein, T., and Kulmala, M.: Aerosol
789 particle formation events and analysis of high growth rates observed above a subarctic
790 wetland-forest mosaic, Tellus, 60(B), 353-365, doi:10.1111/j.1600-0889.2008.00351.x, 2008.

791 Vanhanen, J., Mikkila, J., Lehtipalo, K., Sipila, M., Manninen, H. E., Siivola, E., Petaja, T., and
792 Kulmala, M.: Particle Size Magnifier for Nano-CN Detection, Aerosol Sci. Technol., 45(4),
793 533-542, doi: 10.1080/02786826.2010.547889, 2011.

794 von der Weiden, S. L., Drewnick, F., and Borrmann, S.: Particle Loss Calculator – a new software
795 tool for the assessment of the performance of aerosol inlet systems, Atmos. Meas. Tech., 2(2),
796 479-494, doi: 10.5194/amt-2-479-2009, 2009.

797 Wiedensohler, A., Cheng, Y. F., Nowak, A., Wehner, B., Achtert, P., Berghof, M., Birmili, W., Wu,
798 Z. J., Hu, M., Zhu, T., Takegawa, N., Kita, K., Kondo, Y., Lou, S. R., Hofzumahaus, A., Holland,
799 F., Wahner, A., Gunthe, S. S., Rose, D., Su, H., and Pöschl, U.: Rapid aerosol particle growth and
800 increase of cloud condensation nucleus activity by secondary aerosol formation and condensation:
801 A case study for regional air pollution in northeastern China, J. Geophys. Res., 114(D2), D00G08,
802 doi:10.1029/2008jd010884, 2009.

803 Wang, J., and Wexler, A. S.: Adsorption of organic molecules may explain growth of newly
804 nucleated clusters and new particle formation, Geophys. Res. Lett., 11, 2834-2838, doi:
805 10.1002/grl.50455, 2013.

806 Wang, J., McGraw, R. L., and Kuang, C.: Growth of atmospheric nano-particles by heterogeneous
807 nucleation of organic vapor, Atmos. Chem. Phys., 13(13), 6523-6531, doi:
808 10.5194/acp-13-6523-2013, 2013.

809 Xiao, S., Wang, M. Y., Yao, L., Kulmala, M., Zhou, B., Yang, X., Chen, J. M., Wang, D. F., Fu, Q.
810 Y., Worsnop, D. R., and Wang, L.: Strong atmospheric new particle formation in winter in urban
811 Shanghai, China, Atmos. Chem. Phys., 15(4), 1769-1781, doi: 10.5194/acp-15-1769-2015, 2015.

812 Yu, H., Gannet Hallar, A., You, Y., Sedlacek, A., Springston, S., Kanawade, V. P., Lee, Y. N., Wang,
813 J., Kuang, C., McGraw, R. L., McCubbin, I., Mikkila, J., and Lee, S. H.: Sub-3 nm particles
814 observed at the coastal and continental sites in the United States, J. Geophys. Res., 119(2),
815 2013JD020841, doi: 10.1002/2013jd020841, 2014a.

816 Yu, H., Ortega, J., Smith, J. N., Guenther, A. B., Kanawade, V. P., You, Y., Liu, Y., Hosman, K.,
817 Karl, T., Seco, R., Geron, C., Pallardy, S. G., Gu, L., Mikkilä, J., and Lee, S. H.: New Particle
818 Formation and Growth in an Isoprene-Dominated Ozark Forest: From Sub-5 nm to CCN-Active
819 Sizes, Aerosol Sci. Technol., 48(12), 1285-1298, doi: 10.1080/02786826.2014.984801, 2014b.

820 Yu, F., and Luo, G.: Simulation of particle size distribution with a global aerosol model: contribution
821 of nucleation to aerosol and CCN number concentrations, Atmos. Chem. Phys., 9(20), 7691-7710,
822 doi:10.5194/acp-9-7691-2009, 2009.

823 Yue, D. L., Hu, M., Zhang, R. Y., Wu, Z. J., Su, H., Wang, Z. B., Peng, J. F., He, L. Y., Huang, X. F.,
824 Gong, Y. G., and Wiedensohler, A.: Potential contribution of new particle formation to cloud
825 condensation nuclei in Beijing, Atmos. Environ., 45(33), 6070-6077,
826 doi:10.1016/j.atmosenv.2011.07.037, 2011.

827 Zhang, K. M., and Wexler, A. S.: A hypothesis for growth of fresh atmospheric nuclei, J. Geophys.
828 Res., 107, 4577, doi: 10.1029/2002JD002180, 2002.

829 Zhao, J., Eisele, F. L., Titcombe, M., Kuang, C., and McMurry, P. H.: Chemical ionization mass
830 spectrometric measurements of atmospheric neutral clusters using the cluster-CIMS, J. Geophys.
831 Res., 115, D08205, doi: 10.1029/2009JD012606, 2010.

832 Table 1. Activation diameter ($D_{p,act}$), maximum growth rate in 1.4-3 nm ($GR_{max,\ 1.4\text{-}3}$), overall growth rate in 1.4-3 nm ($GR_{1.4\text{-}3}$), overall growth

833 rate in 3-20 nm ($GR_{3\text{-}20}$), nucleation rate ($J_{1.4}$), condensation sink (CS), and temperature (T) of selected nucleation events. Estimated gas-phase

834 activating vapor concentrations C_∞, pure saturation concentration of activating vapor over flat surface C^*, and Mikkonen H_2SO_4 proxy were

835 shown in right 3 columns. All data were for the time periods with maximum nucleation rates.

836

Type	Date	$D_{p,act}$ (nm)	$GR_{max,1.4\text{-}3}$ (nm h^{-1})	$GR_{1.4\text{-}3}$ (nm h^{-1})	$GR_{3\text{-}20}$ (nm h^{-1})	$J_{1.4}$ ($cm^{-3}s^{-1}$)	T (^oC)	CS ($10^{-2}s^{-1}$)	Mikkonen H_2SO_4 proxy (cm^{-3})	C_∞ (cm^{-3})	C^* (cm^{-3})
A1	May 15, 2014	2.4	6.4	3.6	7.7	3.0×10^{2}	20.8	1.6	8.7×10^{7}	5.1×10^{7}	6.3×10^{6}
A1	Aug 15, 2014	2.4	14.5	7.1	7.7	2.0×10^{2}	26.1	1.8	9.3×10^{7}	1.1×10^{8}	2.5×10^{7}
A2	May 16, 2014	2.4	3.8	1.9	0	95	25.3	1.9	1.4×10^{8}	3.0×10^{7}	4.0×10^{6}
A2	May 20, 2014	2.2	2.9	1.6	0	92	24.1	1.9	3.8×10^{7}	2.3×10^{7}	2.3×10^{6}
B1	Feb 18, 2015	1.6	25.9	4.4	6.0	1.1×10^{3}	8.2	3.3	3.9×10^{7}	1.7×10^{8}	3.5×10^{7}
B1	Dec 27, 2014	1.6	17.7	4.2	5.5	1.9×10^{2}	7.6	2.8	3.5×10^{7}	1.2×10^{8}	2.8×10^{7}
B2	Feb 19, 2015	1.9	25.0	8.9	10.1	8.0×10^{2}	7.4	3.2	3.7×10^{7}	2.0×10^{8}	5.7×10^{7}

B2	Mar 4, 2015	1.9	18.0	5.8	8.7	2.5×10^{3}	3.9	2.2	4.8×10^{7}	1.4×10^{8}	2.0×10^{7}

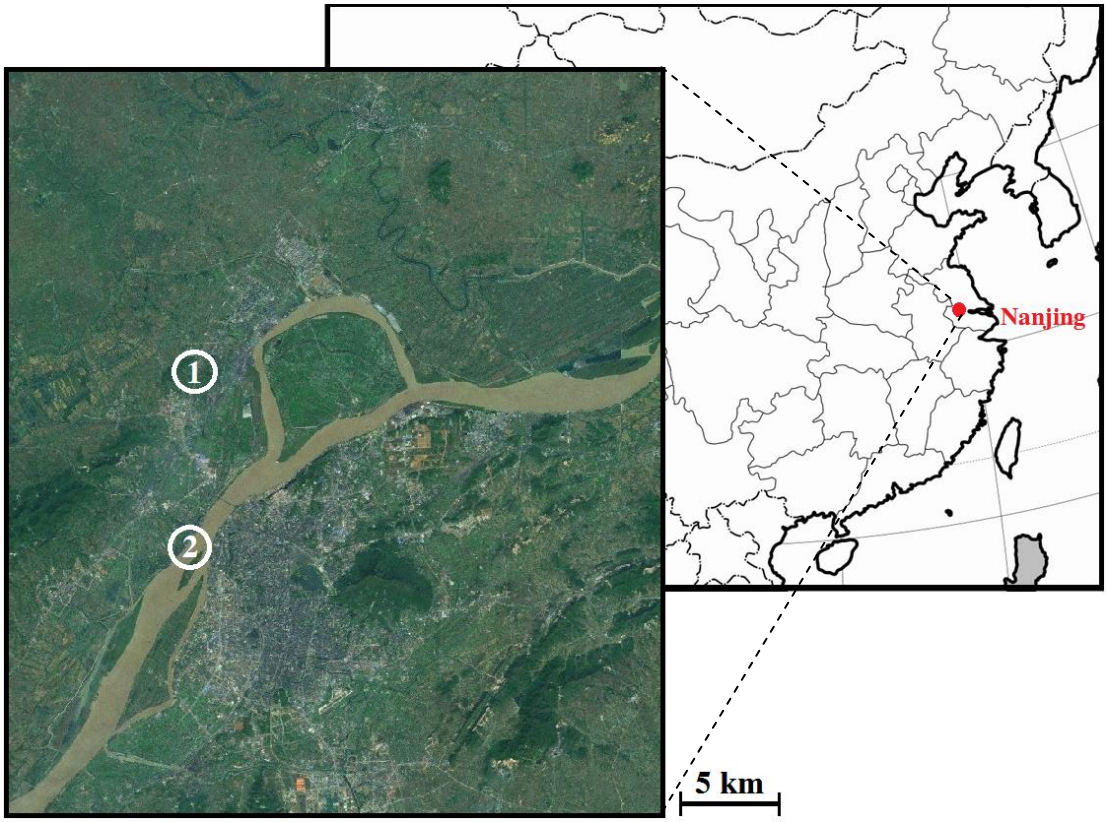

Figure 1. Locations of two urban measurement sites in Nanjing, the second largest megacity in the Yangtze River Delta region, China. ① is the NUIST site and ② is the summer measurement site.

842

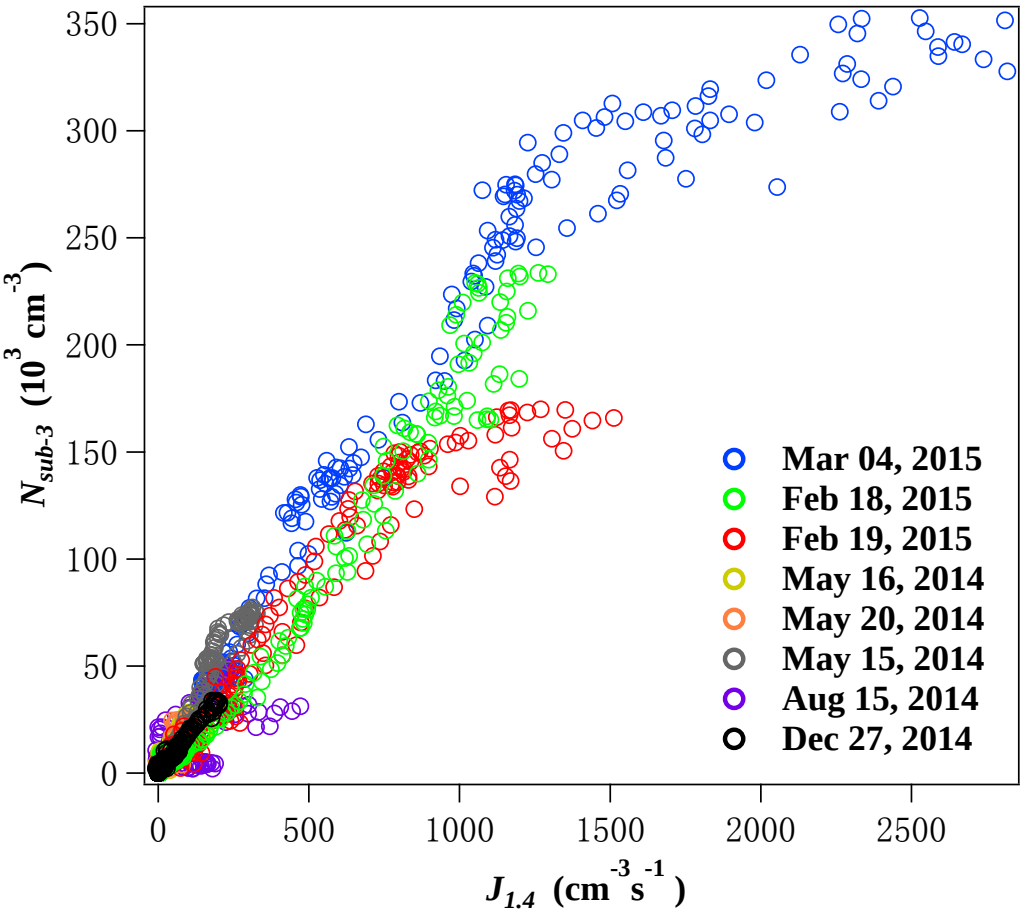

843

844 Figure 2. $N_{sub\text{-}3}$ *vs.* $J_{1.4}$ in the 8 nucleation events in February, May, December and August during

845 2014-2015. The events were indicated by different colors (blue: March 1, 2015; green: February

846 18, 2015; red: February 19, 2015; purple: August 15, 2014; black: December 27, 2014; grey:

847 May 15, 2014; orange: May 20, 2014; yellow: May 16, 2014)

848

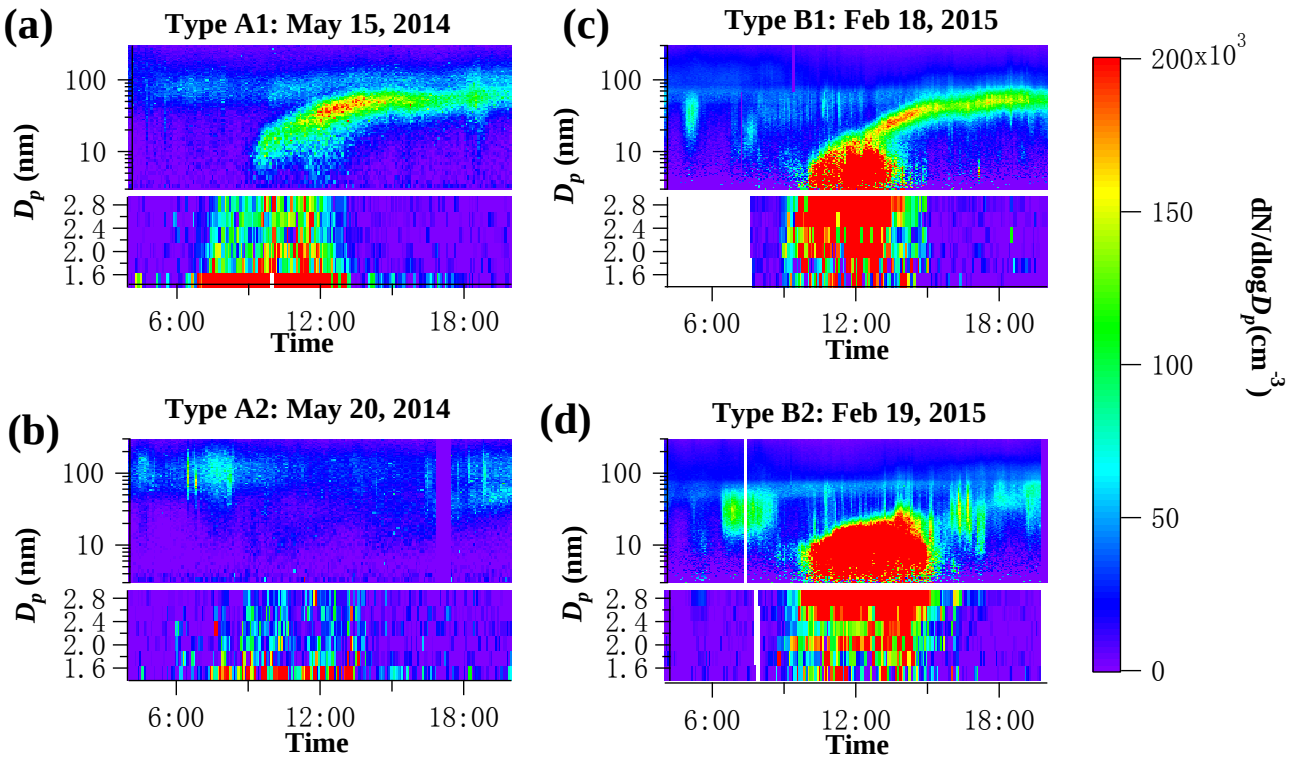

Figure 3. Size spectra of typical (a) Type A1 event on May 15, 2014; (b) Type A2 event on May 20, 2014; (3) Type B1 event on February 18, 2015 and (d) Type B2 event on February 19, 2015 during our measurement period. Size spectra from 3-300 nm (logarithmic scale) and 1.4-3 nm (linear scale) were obtained using SMPS and nCNC, respectively.

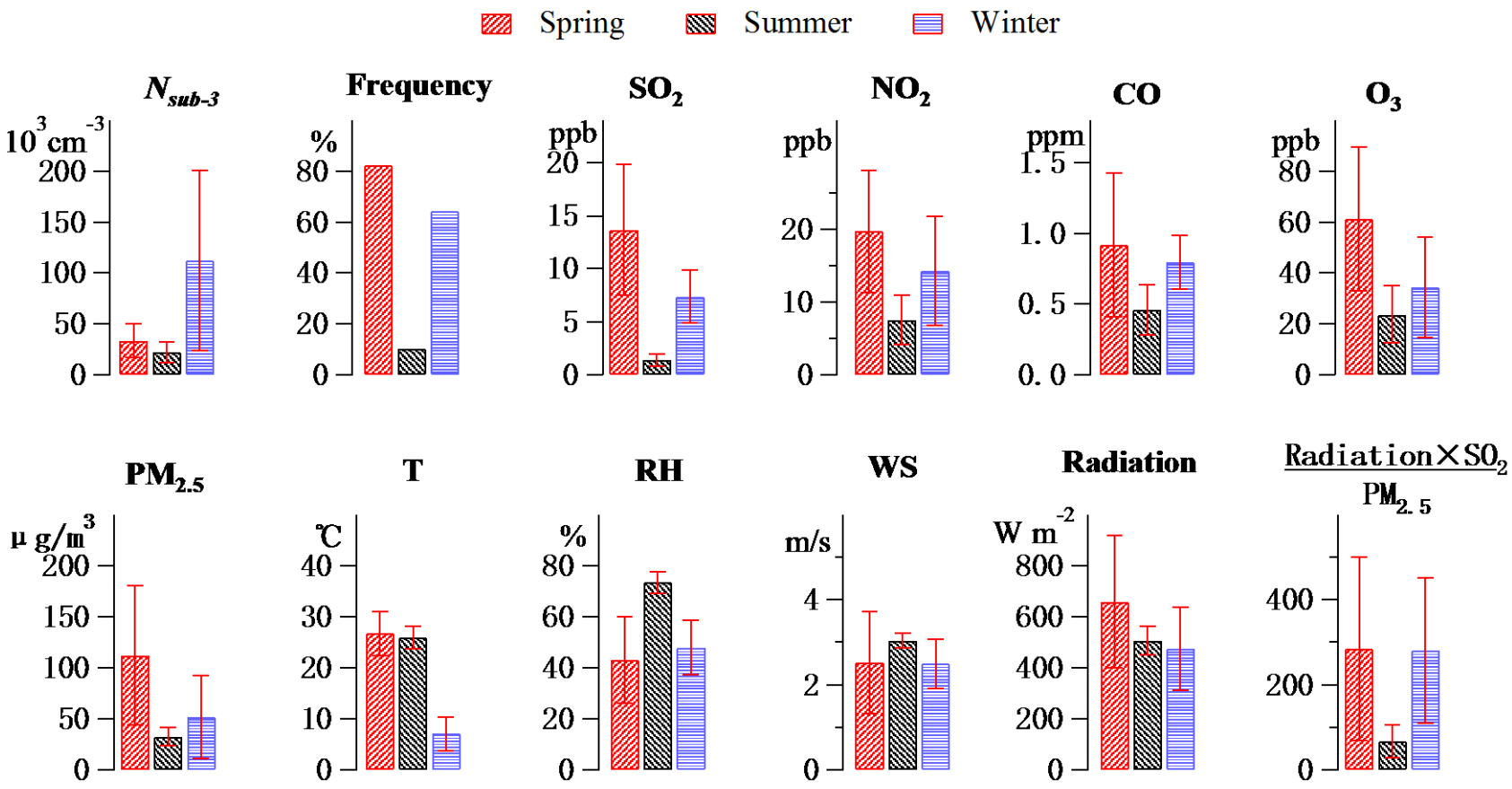

Figure 4. Mean and standard deviation of event-averaged N_{sub-3}, anthropogenic trace gases (SO_2, NO_2, CO and O_3), $PM_{2.5}$, and meteorological variables (temperature, RH, wind speed (WS), solar radiation, and radiation ×SO_2/$PM_{2.5}$) for nucleation events in spring (n=17), summer (n=3) and winter (n=14). Nucleation frequency (the percentage of event days out of total measurement days) was also shown.

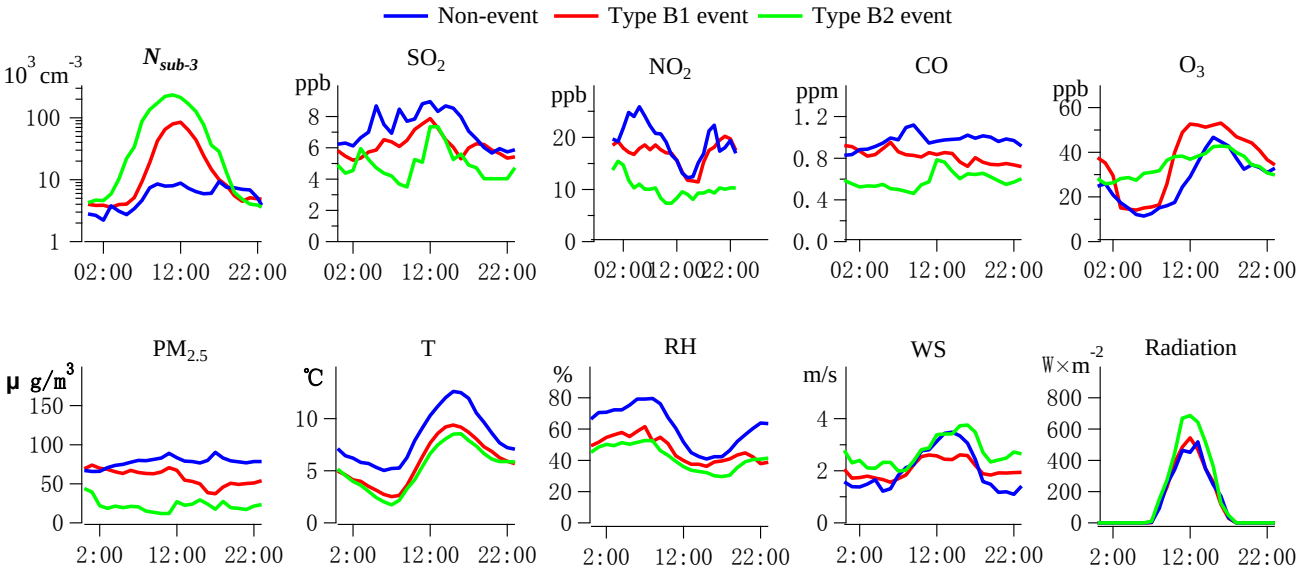

Figure 5. Diurnal variations of mean N_{sub-3}, anthropogenic trace gases (SO_2, NO_2, CO and O_3), $PM_{2.5}$, and meteorological variables (temperature, RH, wind speed, and solar radiation flux) on non-event days (n=8, blue line) and event days (n=3 for Type B1 event, red line and n=6 for Type B2 event, green line) during winter measurement period.

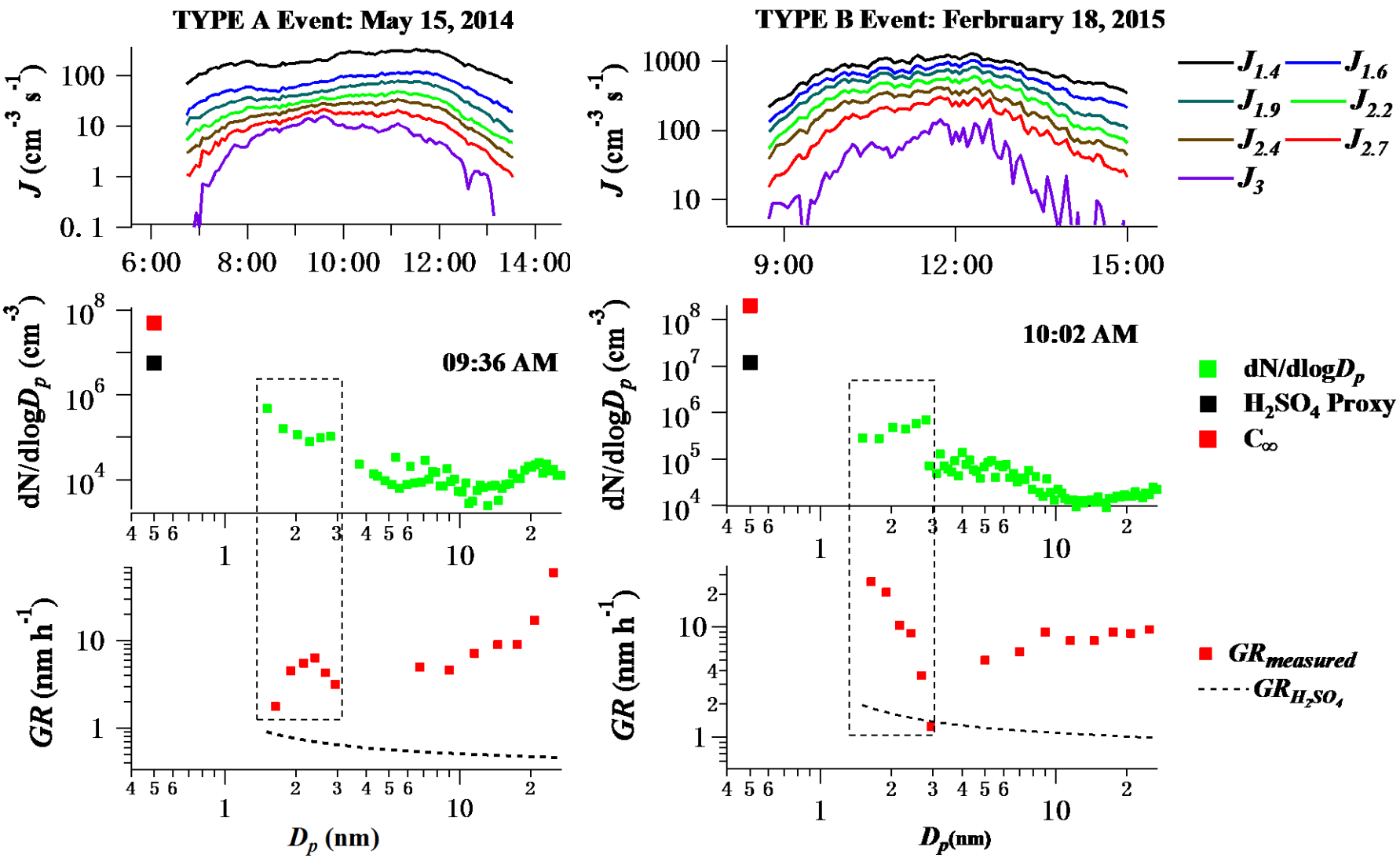
TYPE A Event: May 15, 2014
TYPE B Event: Ferbruary 18, 2015
J (cm-3 s-1)
100
10
1
0. 1
6:00
8:00
10:00
12:00
14:00
1000
100
10
9:00
12:00
15:00
J1.4
J1.6
J1.9
J2.2
J2.4
J2.7
J3
dN/dlogDp (cm-3)
09:36 AM
10:02 AM
dN/dlogDp
H2SO4 Proxy
C∞
GR (nm h-1)
GRmeasured
GRH2SO4
Dp (nm)

866

867 Figure 6. Upper: formation rates (or equivalently, particle growth fluxes) of 1.4, 1.6, 1.9, 2.2, 2.4, 2.7 and 3.0 nm cluster/particles on May 15
868 2014 (Type A1 event) and Feb 18 2015 (Type B1 event). Middle: particle size distribution (dN/dlogD_p, green square) selected during the two
869 events (9:36 AM and 10:02 AM). Lower: particle growth rates measured during the same time periods ($GR_{measured}$, red square). Also shown in
870 the figure were H_2SO_4 proxy (black square) and growth rates calculated from the H_2SO_4 proxy (GR_{H2SO4}, dashed black line), as well as the
871 calculated ELVOC concentration (C_∞, red square) during the same time periods. Dashed boxes in the lower panels highlighted the size
872 distributions and growth rates between 1.4 and 3 nm measured with nCNC.

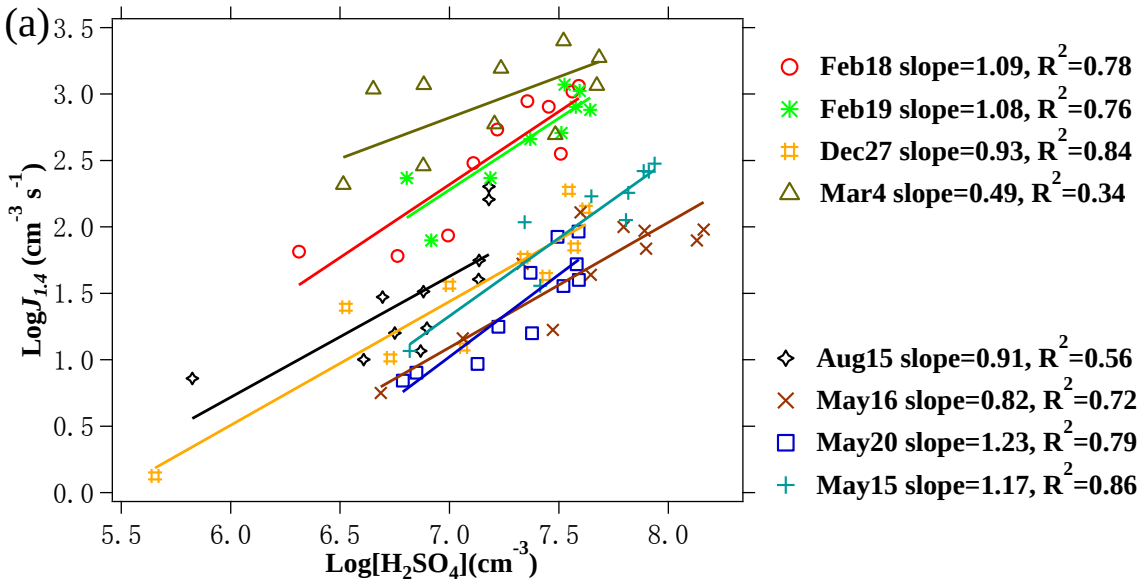

873

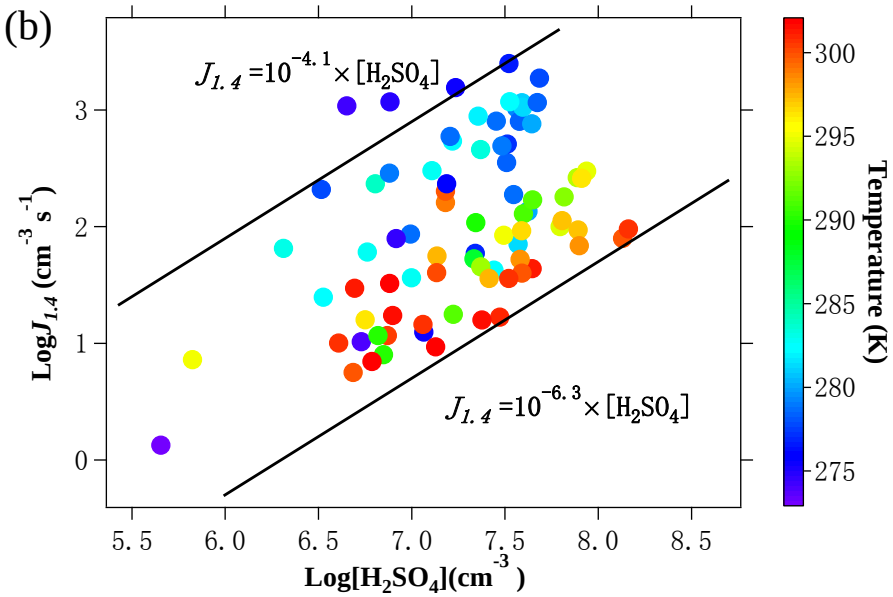

874

875 Figure 7. (a) Correlations between log $J_{1.4}$ and log [H_2SO_4] for the 8 events. H_2SO_4 proxy was
876 calculated according to Mikkonen et al. (2011). $J_{1.4}$ and [H_2SO_4] were synchronized to 1 hour that
877 was the time resolution of solar radiation data. The colored lines showed linear fits to the data of
878 every single event. (b) The same dataset as (a), but with symbol color to indicate ambient
879 temperature. Two black lines showed the linear dependences of $J_{1.4}$=10$^{-4.1}$ × [H_2SO_4] and $J_{1.4}$=10$^{-6.3}$ ×
880 [H_2SO_4], between which most of data points located.

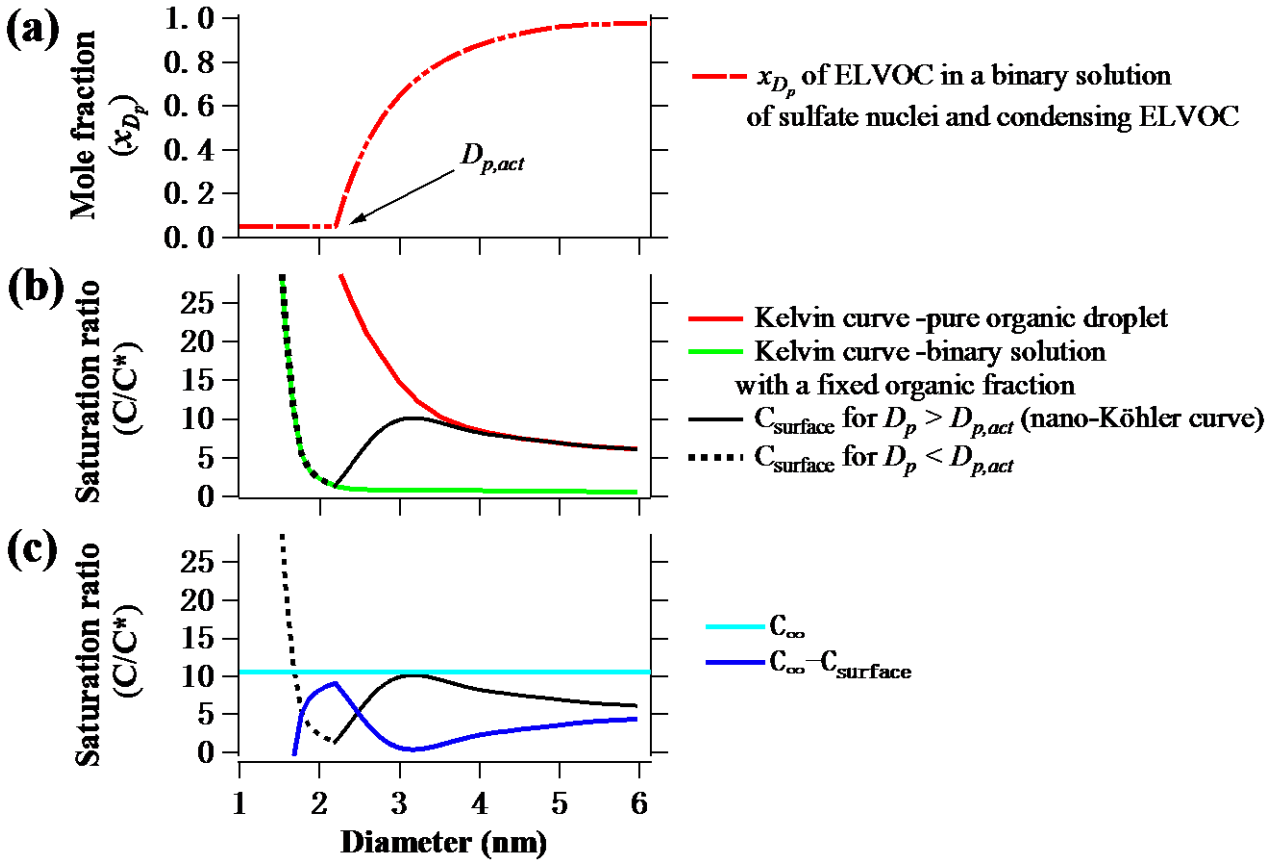

881

882 Figure 8. (a) mole fraction of organics (x_{D_p}) in a binary solution of sulfate nuclei and activating

883 organics (ELVOC) in a new particle. Nuclei activation diameter $D_{p,act}$ is the size where ELVOC

884 begins to dilute the nuclei. A fixed organic fraction of 5% was plotted, for simplification, in the

885 particle before activation. (b) Kelvin equilibrium curves over a pure organic droplet (red line) and a

886 binary solution with a fixed organic fraction (green line), nano Köhler curve for $D_p > D_{p,act}$ (black

887 solid line) and surface concentration $C_{surface}$ for $D_p < D_{p,act}$ (black dashed line). (c) gas phase

888 concentration of the organic vapor (C_∞, cyan line), surface concentration C_∞ (black line), and

889 $C_\infty - C_{surface}$ (blue line).

890

891

892

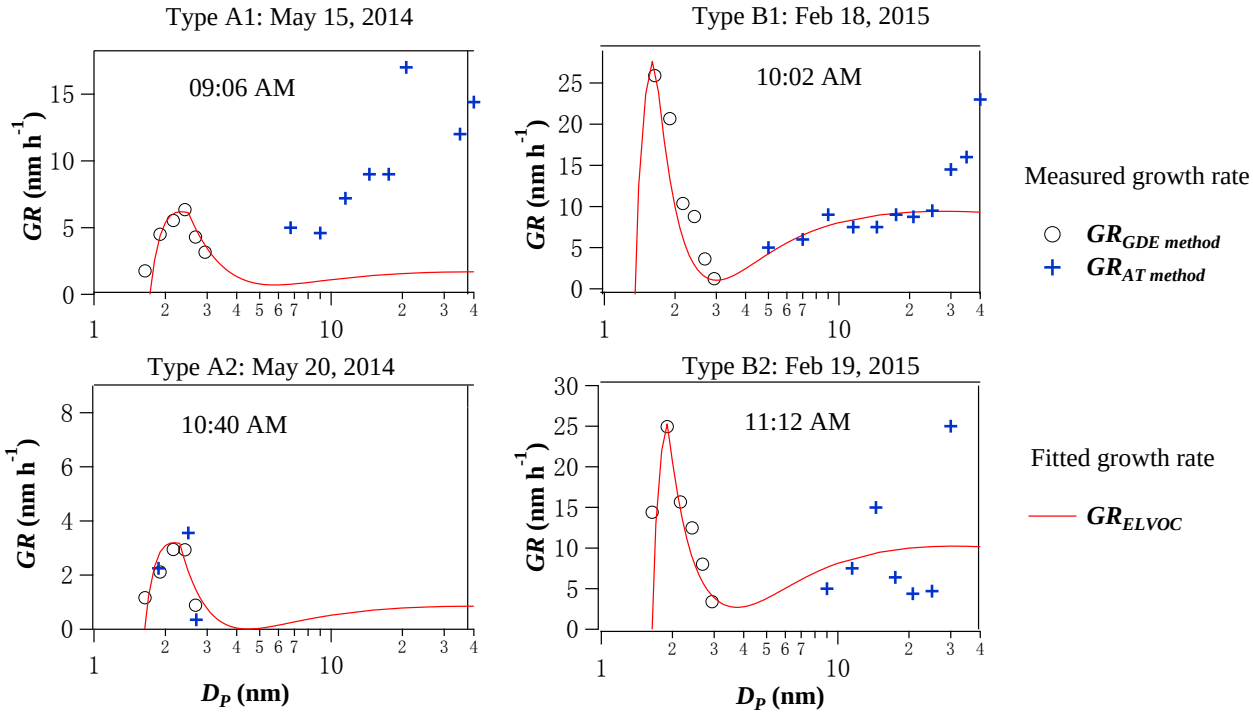

893

894

895 Figure 9. Comparisons of measured ($GR_{GDE\ method}$, black circle) and fitted (GR_{ELVOC}, red line) growth

896 rates from Eq. (4) for typical Type A1, A2, B1, and B2 events. Also shown were growth rates

897 calculated from appearance time method ($GR_{AT\ method}$, blue cross) for sub-3 nm particles when growth

898 rate was relatively small or for larger particles with large size intervals.

899